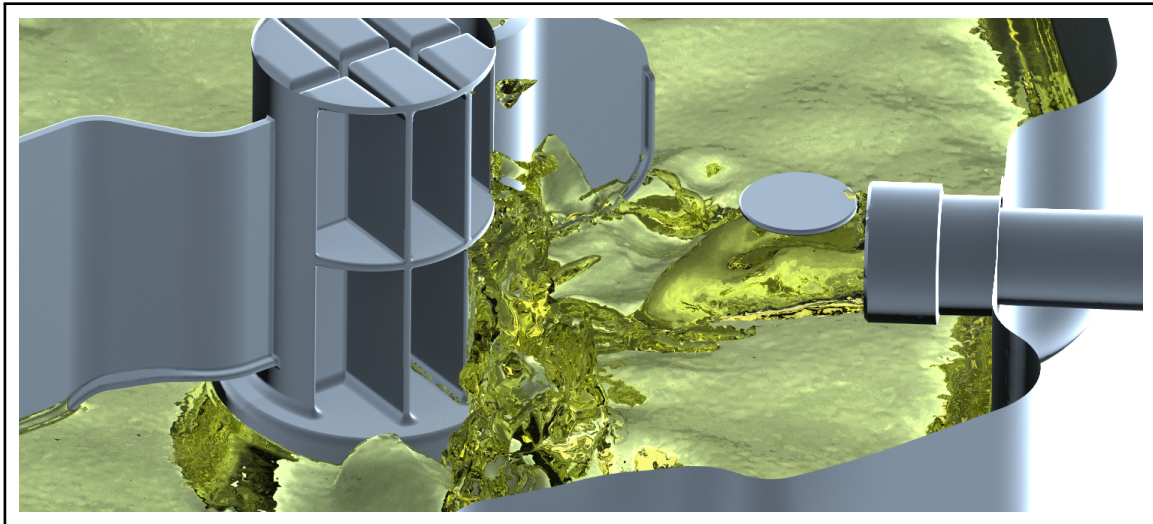# One- and Three-Dimensional CFD Study of an Onboard Refuelling Vapour Recovery System

Implementation and Evaluation of an Evaporation Model

Master's thesis in Applied Mechanics

Henrik Johansson
Andreas Wikström

One- and Three-Dimensional CFD Study of an Onboard Refuelling Vapour Recovery System

Implementation and Evaluation of an Evaporation Model

HENRIK JOHANSSON & ANDREAS WIKSTRÖM

Department of Mechanics and Maritime Sciences
Division of Fluid Dynamics
CHALMERS UNIVERSITY OF TECHNOLOGY
Göteborg, Sweden 2020

One- and Three-Dimensional CFD Study of an
Onboard Refuelling Vapour Recovery System
Implementation and Evaluation of an Evaporation Model
HENRIK JOHANSSON & ANDREAS WIKSTRÖM

Cover: Visualization of fuel entering the fuel tank, constructed in Star-CCM+.

One- and three-dimensional CFD study of an Onboard Refuelling Vapour Recovery System
Implementation and Evaluation of an Evaporation Model
Master's thesis in Applied Mechanics
HENRIK JOHANSSON & ANDREAS WIKSTRÖM
Department of Mechanics and Maritime Sciences
Division of Fluid Dynamics Chalmers University of Technology

Abstract

The human impact of the environmental development is without doubt one of the biggest challenges in modern society. The influence from cars is highly debated and especially the impact from fossil fuels like gasoline. At the Fuel System Department at Volvo Cars in Torslanda, the refuelling process of the cars is tested with physical experiments on a daily basis. A system called Onboard Refuelling Vapour Recovery (ORVR) works within the fuel system to prevent hydrocarbons and other harmful particles to escape during refuelling. Countries set different limitations on what quantity of particles that may be emitted and it is sometimes difficult to explain what causes variations in the results of the experiments. Computational fluid dynamics (CFD) is used in order to get a more detailed view of the ORVR system, which could be a great complement to physical experiments. Decisive parameters for the flow field could then be evaluated and possible sources of errors of the testing could be discovered.

In this thesis the ORVR system is studied through both one- and three-dimensional computational fluid dynamics. The studied refuelling system corresponds to the fuel system for a Volvo XC90 certified for the US market, with a 71 liters fuel tank. The three dimensional case is simulated in SIEMENS Star-CCM+. The simulation uses the Volume of Fluid (VOF) model for surface tracking of the multiphase problem. An evaporation model is implemented to deal with the mass transfer between the phases. The accuracy of the rate of evaporation of the gasoline is studied by both experimental and computational testing.

Since the three-dimensional simulations are computationally expensive and time consuming, a one-dimensional study is also performed, where the software GT-Suite is used. The geometry is discretized from the three-dimensional CAD models to a one-dimensional system using softwares like ANSA, GT SpaceClaim and GEM3D before being imported into GT-Suite.

The results from the different approaches are then evaluated and compared with experimental data. Possible advantages and drawbacks with the respective methods are analyzed and presented in a perspicuous way to the company.

Keywords: Evaporation, ORVR, CFD, Star-CCM+, GT-Suite, Gasoline, Refuelling, Multiphase flow, Emissions, Fuel system.

Nomenclature

AMG   Algebraic Multigrid
BC   Boundary Condition
CAD   Computer Aided Design
CFD   Computational Fluid Dynamics
CFL   Courant-Friedrichs-Lewy condition
CV   Control Volume
EPA   Environmental Protection Agency
EVAP Evaporation
FDM Fuel Delivery Module
FLVV Fill Limit Vent Valve
FVM Finite Volume Method
HRIC High Resolution Interface Capture
LCO Liquid Carry Over
LES   Large Eddy Simulation
ORVR Onboard Refuelling Vapour Recovery
VOF   Volume Of Fluid
α Volume fraction
Γ General constant
γ Colour function
κ Von Karman constant
λ Heat conductivity
μ Dynamic viscosity
ν Kinematic viscosity
Φ General variable
ρ Density
τ Stress
Δt Time step
Δx Cell size
$\dot{h}$ Source term
$\dot{m}_i$ Rate of evaporation of component
$\dot{M}_{i,c}$ Approximated evaporation rate for one cell
$\mathbf{f}$ Body forces
$\mathbf{g}$ Gravity
$\mathbf{T}$ Stress tensor
$\mathbf{u}$ Velocity
C_μ Property of the flow
c_p Specific heat capacity

Co	Courant number
D_i	Diffusion coefficient of component
E	Specific energy
F_σ	Surface tension force
$F_{\text{wall adhesion}}$	Wall adhesion force
i	Internal energy
k	Thermal conductivity
N_v	Number of evaporating components
p	Pressure
p^*	Vapour pressure
S	Source term
T	Temperature
t	Time
u	Velocity in x-direction
u^+	Dimensionless speed
u_r	Friction velocity
v	Velocity in y-direction
W	Molar weight
w	Velocity in z-direction
X_i	Molar fraction of component
y^+	Dimensionless wall distance
Y_i	Component mass fraction
^{s}	surface
$_{bg}$	background
$_E$	of the energy equation
$_g$	gas phase
$_l$	liquid phase
$_{M_x}$	x-component of the momentum equation

Contents

Contents

Preface

This thesis is a continuation of last years Master's Thesis conducted at the Fuel System Department at Volvo Cars, which lacked a model for evaporation of the fuel. The purpose of performing computational fluid dynamics of the Onboard Refuelling Vapour Recovery system is to get a better understanding of the fuel flow phenomena occurring in the system, as well as being a possible complement to the physical experiments performed on a daily basis at the company.

The implementation of evaporation of the investigated fuel proved to be a complex problem in the three-dimensional simulation, where no solution of how to compute the measured saturation pressure of the fuel was found during the time of the project. The saturation pressure was therefore limited to be the default values of gasoline inbuilt in the software Star-CCM+, which causes some uncertainties when comparing the results to experimental data measured with another saturation pressure of the fuel.

A one-dimensional simulation setup of the system was also conducted during the project. This might be an effective tool for the company in order to get quick results for understanding the effect of changes of system inputs.

Acknowledgements

Henrik Johansson & Andreas Wikström, Gothenburg, June 2020

List of Figures

List of Tables

1
Introduction

This thesis treats the implementation of an evaporation model when investigating a fuel tank, using the softwares Star-CCM+ and GT-Suite before comparing the results towards experimental testing. The work was conducted at the Fuel System Department at Volvo Cars Corporation in Torslanda, Gothenburg.

1.1   Background

The awareness of environmental issues has increased significantly the most recent years with the car being a symbol for the human influence of the planet's health. The society sets restrictions for car manufacturers to limit emissions in order to reduce damage of the nature. When refueling a car, it is possible for hydrocarbon vapours to escape due to evaporation. Hydrocarbons have a negative effect on both environment and human health. Because of this, a system is needed to collect the hydrocarbons. In Europe this system is implemented into the fuel station, whereas in the United States a system is put into the car. This system is called ORVR (Onboard Refuelling Vapour Recovery). These emissions can also escape when the tank is sloshing, therefore, it is important to include the effect of evaporation when evaluating the performance of the system.

1.2   Purpose of the study

Experimental testing has been a fundamental method during many years when investigating design changes of the ORVR system at the Fuel System Department at Volvo Cars Corporation. Performing physical experiments demands time and resources, which makes computer aided simulations a desirable approach for evaluation. Simulations also allows for quicker evaluation of changes to the system compared to waiting for new physical components to be made and tested. The purpose of the Master's Thesis is to further develop a reliable simulation setup for the ORVR system by including a model for evaporation of the gasoline, while keeping the required time as short as possible.

1.3   Objectives

The aim with the study is to model and implement the effect of evaporation into existing models to evaluate the performance and design of the ORVR system virtually,

and by that reduce the need of physical experiments. To validate the performance of the implemented model, experiments were held at a laboratory. The CFD simulations in three dimensions are slow, therefore a one-dimensional solver setup was also created to increase the available options of approaches and to be able to save computational time.

1.4   Limitations

In order to model the physics in the ORVR system, some assumptions were made to decrease the required simulation time. The air was assumed to be an ideal gas while the liquid was assumed incompressible and non-reacting. General limitations during the study are listed below:

- Computational resources are limited, with a cluster consisting of 200 cores available.
- The studied fuel is gasoline, see Appendix A.1.
- The resources and time available at the laboratory are limited.
- The total time is limited to 20 weeks which corresponds to 30 credits per student.
- The software used is a limiting factor of what is possible to do and what options are possible to investigate.
- No new models were developed, only existing models were used.
- The Fill Limit Vent Valve (FLVV) is not modelled.
- The Carbon Canister was replaced by a pressure drop in the simulations, meaning no adsorption of hydrocarbons were modelled.

2

Theory

This chapter explains the different theoretical subjects that are required for understanding the other parts of the thesis.

2.1 Geometry of fuel system

The fuel system consists of a number of parts all required to fill some role. They are either fundamental parts such as the fuel pump or the tank itself, or the other parts needed to meet regulations and limit emissions such as the canister and leak detection pump. A CAD illustration of the fuel tank geometry and other in-going parts of the ORVR system are shown in Figure 2.1.

2.1.1 Fuel pistol and capless filler neck

The capless filler neck is the part of the fuel distribution system that is visible from outside the car when opening the refuelling door. The fuel pistol, connected to the pump at the refuelling station, is attached to the capless filler neck when refuelling and gasoline is fed into the car's fuel system. The filler neck being capless implies that there is no cap to unscrew from the unit, the pistol is instead put straight into it. Some inbuilt features obstructs a pistol with the wrong geometry to enter. This prevents filling of the tank with an inappropriate fuel. In Europe the fuel pistol also collects the vapours that are displaced out of the tank when refuelling. In the United States however, this responsibility is put on the car and a built-in system is implemented, the ORVR system [1].

2.1.2 Fuel filler pipe

The fuel filler pipe transports the fuel from the filler neck to the fuel tank. The design of this pipe is of importance to avoid excessive evaporation due to turbulence. It is also important to design to avoid other phenomena such as spit-back, where fuel is spat out of the filler cap and into the surroundings and onto the user, holding the fuel pistol [1].

2.1.3 Fuel tank

The fuel tank is where the fuel is stored between refuelling and being used in the engine. This certain design is shaped like a saddle, leaving room for the drive

shaft for four wheel drive vehicles. Because of this the tank is divided in two sides, separated when the fuel level is low. One side is where the fuel enters and where the fuel delivery module (FDM) is positioned, this is called the active side. The other side is called the passive side [1].
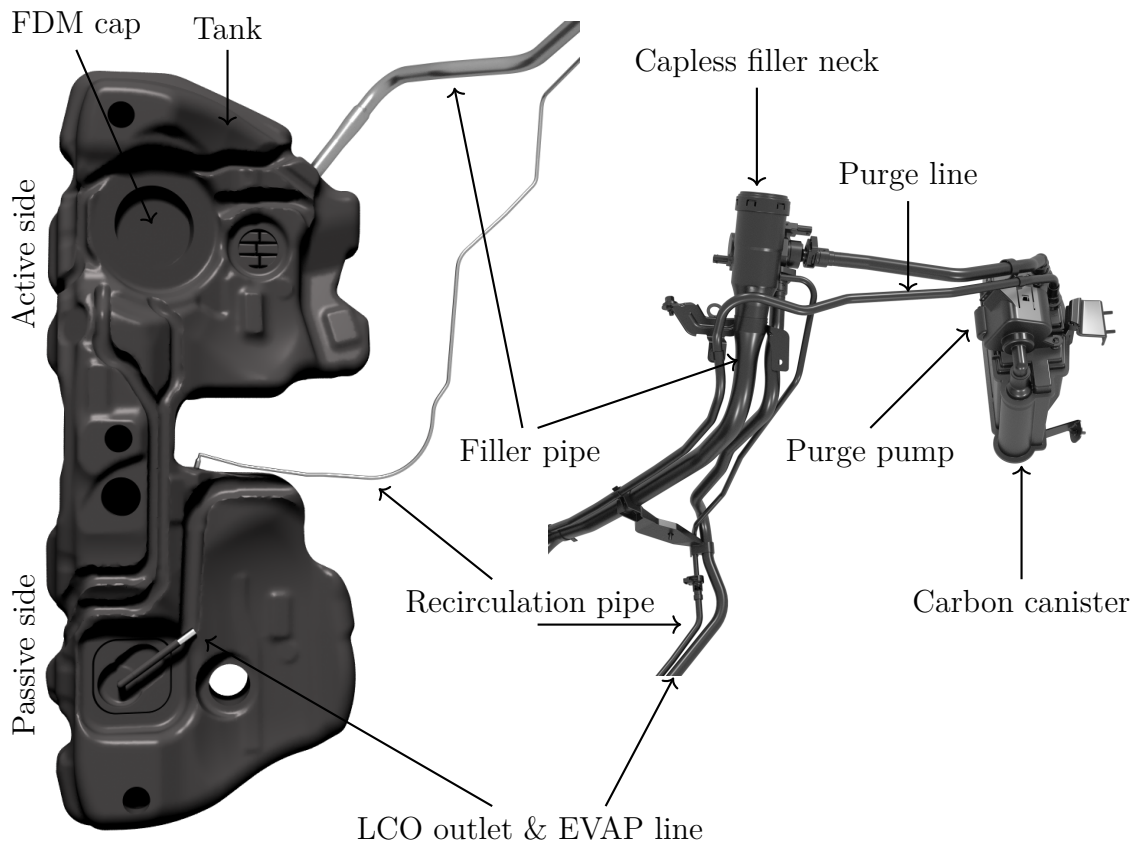
Figure 2.1: The fuel system with the most important elements pointed out. The figures are viewed from above and the right-hand-side figure is the continuation of the filler pipe cut off on the left-hand-side figure.

2.1.4 Fill limit vent valve

In the fuel tank there is a component called Fill Limit Vent Valve (FLVV). The purpose of this valve is to enable the displaced gas inside the tank to escape, but prevent the fuel from escaping the same way. When refuelling, and the tank is not full, the valve is open and the gases can escape from the tank. However, when the fuel tank is filled close to its limit a floater in the valve rises with the liquid and closes the valve shut. Now there is nowhere for the displaced air to escape and as such, the pressure rises fast. The refuelling is shut off shortly after this happens [1].

2.1.5 Recirculation/Leak detection line

The recirculation or leak detection line serves two purposes in the fuel system. During refuelling the pipe acts as an extra way to evacuate the displaced air and gas inside he tank. The gas follows the recirculation line to the filler neck where it

follows the fuel flow back into the tank. This reduces the load on the canister which decreases the requirements on it and therefore the cost. When not refuelling, the line is used for leak detection. After the car is turned off, the leak detection pump sucks air and gas from the tank, through the leak detection line, and can detect if there is a leakage. This is done because of legal regulations on leakages from the entire fuel system [1].

2.1.6 EVAP and purge lines

The EVAP line connects the fuel tank and the carbon canister where the gas containing air and hydrocarbons travels. From the canister, the gas travels via the purge line towards the engine where the combustion takes place [1].

2.1.7 Carbon canister

To prevent hydrocarbon emissions into the environment a sort of filter is put between the tank vent system and the outside world. This filter is called the Carbon Canister. It contains activated carbon that adsorbs hydrocarbons and lets through air. The canister can adsorb about as much hydrocarbons as passes through it during one refuelling and must be cleaned between refuellings. This is done through a process called purging. During purging air is passed through the canister bringing the hydrocarbons away [1].

2.1.8 Purge valve

The purge valve is the valve opening the purge lines to the lower pressure of the engine. This creates a suction of air throughout the purge system bringing hydrocarbons from the canister to the engine for combustion. This effectively cleans the canister of hydrocarbons and prepares it for the next refuelling [1].

2.1.9 Test procedure of the ORVR system

The test procedure of the ORVR system was proposed by the American Environmental Protection Agency (EPA) in 1993. They proposed the test to be begun with a 6 to 24 hour soaking period in 27°C to stabilize the temperature in the fuel tank. The tank is filled to 10% of it nominal volume with a certification fuel during this period. The tank is then placed in an environmentally closed room and filled with fuel at 19.4°C at a rate of typically 15-38 liters per minute, until the first nozzle shut off. If the tank is not filled above 85% of nominal tank volume the filling is restarted. This is repeated until 95% of the tank volume is filled [2].

2.2 Computational fluid dynamics

The computational fluid dynamics applied within the project are described below.

2.2.1   Governing equations

The governing equations of fluid dynamics are based on three fundamental principles:

- Conservation of mass: Mass can neither be created nor destroyed.
- Newtons second law: The force of an object is equal to its mass times its acceleration.
- Conservation of energy: Energy can neither be created nor destroyed. [3]

One assumption needed for these principles is that there is no reaction occurring in the fluid. Both molecular and subatomic reactions would create discontinuity in both conservation of mass and energy when mass is converted into energy and vice versa.

The conservation of mass in the system is described by the continuity equation, which could be written as Equation 2.1 for an unsteady and compressible fluid in three dimensions.

$$\frac{\partial \rho}{\partial t} + div(\rho \boldsymbol{u}) = 0 \tag{2.1}$$

The momentum conservation, which corresponds to the equality of the rate of change of momentum and the sum of forces on a fluid particle, can be written as Equation 2.2 for the x-component of the momentum equation.

$$\rho \frac{Du}{Dt} = \frac{\partial(-p + \tau_{xx})}{\partial x} + \frac{\partial \tau_{yx}}{\partial y} + \frac{\partial \tau_{zx}}{\partial z} + S_{M_x} \tag{2.2}$$

Equation 2.2 could be written in the same manner for the y- and z-direction as well [4].

The conservation of energy is described as the equality between the rate of change of energy and the sum of the rate of heat addition together with the rate of work performed on a fluid particle. This relationship corresponds to the energy equation, Equation 2.3.

$$\rho \frac{DE}{Dt} = -div(p\boldsymbol{u}) + \frac{\partial}{\partial x_j} + div(k \ grad \ T) + S_E \tag{2.3}$$

The left hand side of Equation 2.3 relates to the rate of increase of energy of a fluid particle per unit volume, where E is the specific energy of a fluid defined as

$$E = i + \frac{1}{2}(u^2 + v^2 + w^2)$$

where i is the sum of internal energy and $\frac{1}{2}(u^2 + v^2 + w^2)$ represents the kinetic energy of the fluid. The two first terms of the right hand side of Equation 2.3 relates to the rate of work done on a fluid particle, the third term of the same equation corresponds to the net rate of heat added to a fluid particle while the last term, S_E, is the source term [4].

The derived equations regarding the conservation principle have significant commonalities. By introducing a general variable ϕ for various scalar quantities, all the governing equations could be written as a single transport equation, shown in Equation 2.4.

$$\frac{\partial(\rho\phi)}{\partial t} + div(\rho\phi\boldsymbol{u}) = div(\Gamma\ grad\phi) + S_\phi \tag{2.4}$$

This transport equation for the property ϕ is used as a starting point when using the finite volume method (FVM), which is the used spatial discretization scheme during this study. The computational domain is divided into a finite number of discrete control volumes (CV). By integrating the transport equation over the control volumes and using Gauss's divergence theorem, the discretized form of the governing equations are gained and can hence be solved for each CV in the flow field [4].

2.2.2 Time discretization

When running a multiphase transient simulation, the implicit unsteady time integration scheme is the only available time integration scheme in Star-CCM+. It treats time scales of either the same order as the convective/diffusive processes or if it is related to relatively low external excitation [5], which makes it suitable for this study.

When using the implicit unsteady approach, the time step must be defined. This could advantageously be done with respect to the Courant-Friedrichs-Lewy (CFL) condition, further explained in Section 2.2.2.1. It is also possible to choose the order of the scheme and set the number of inner iterations, which both can affect the required computational time as well as the accuracy of the simulations [5].

2.2.2.1 The Courant-Friedrichs-Lewy (CFL) condition

The CFL condition is used to give an upper limit to the local time step, aiming to ensure a stable and converging simulation. The CFL condition is defined as

$$C_o = \Delta t \frac{v_i}{\Delta x_i} \leq C_{CFL} \tag{2.5}$$

where v is the local maximum speed in the CV, Δt the local time step and Δx the length of the computational element. It is although important to note that the local time step constraint does not necessarily ensure that the CFL condition is satisfied since the CFL condition is non-local. To be sure that the condition is satisfied in the entire domain, it could be implemented globally by using the largest speed and the corresponding smallest time step in the computational domain [6].

2.2.2.2 Adaptive time step

In the latter versions of Star-CCM+, there is a possibility to choose a method for an adaptive time step using the CFL condition. The solver then automatically controls the time step in order to optimize the demanded computational time without diminishing the accuracy and convergence of the simulation. It is nevertheless important

to choose an appropriate model for the adaptive time step to the studied flow field to generate reliable results. This is further explained in Section 3.1.2

2.2.3 Turbulence modelling

The fuel flow in the ORVR system is, like almost all other fluid flows encountered in the daily life, turbulent in its nature. This means that the flow is irregular and chaotic in its behaviour. The movement could be described by the Navier-Stokes equation, Equation 2.6.

$$\rho\frac{\partial\phi_i}{\partial t} + \rho\frac{\partial\phi_i\phi_j}{\partial x_j} = -\frac{\partial p}{\partial x_i} + \frac{\partial}{\partial x_j}\left(\mu\frac{\partial\phi_i}{\partial x_j}\right) \tag{2.6}$$

The scalar property studied in the governing equations could be divided via the Reynolds decomposition into a mean part and a fluctuating part. The decomposition is written as

$$\phi_i = \overline{\phi_i} + \phi_i'$$

where the overlined symbol defines the time averaged value according to

$$\overline{\phi} = \frac{1}{2T}\int_{-T}^{T} v dt$$

while the symbol with a prime represents the unsteady fluctuating part [7].

The decomposition is done since the mean values of the studied quantity often are of more interest than their time histories. When solving the decomposed time averaged governing equations of the flow field, unknown terms for the turbulent stresses appear that has to be closed. Since it is computationally expensive to solve the governing equations of a turbulent flow field, a turbulence model is needed to generate values of the closure problem linked with the unknown variables. How this is done depends on the studied flow field and the available computational resources, why it is important to carefully investigate which model to use [7].

2.2.3.1 Reynolds averaged Navier-Stokes

One way of modelling all turbulent scales is to solve the Navier-Stokes equation, Equation 2.6, by applying the Reynold decomposition, Equation 2.2.3, of the scalar field of interest. This results in Equation 2.7

$$\rho\frac{\partial\overline{\phi}_i\overline{\phi}_i}{\partial x_j} = -\frac{\partial\overline{p}}{\partial x_i} + \frac{\partial}{\partial x_j} + \left(\mu\frac{\partial\overline{\phi}_i}{\partial x_j} - \rho\overline{\phi_i'\phi_j'}\right). \tag{2.7}$$

The unknown term is the Reynolds stress tensor, $\rho\overline{\phi_i'\phi_j'}$, which needs to be modeled. This could be done by applying a suitable eddy-viscosity model [7].

2.2.3.2 The realizable $k - \epsilon$ model

The $k - \epsilon$ eddy viscosity model solves the modelled transport equations for the turbulent kinetic energy (k) and the turbulent dissipation rate (ϵ) in order to determine the turbulent eddy viscosity according to

$$\nu_t = C_\mu \frac{k^2}{\epsilon}.$$

The Realizable $k - \epsilon$ model includes a new equation for the turbulent dissipation rate (ϵ) and C_μ is expressed as a function of the properties of the flow field instead of being assumed a constant in the original $k - \epsilon$ eddy viscosity model, which increases the realizability [7][8].

2.2.4 Wall treatment

When refuelling a car, the fuel must pass the complex geometry of the ORVR system described in Section 2.1. The geometry is interpreted as walls in the simulation setup and is a source of vorticity in the flow field. It is important to capture the behaviour of the flow in the near wall regions, which requires a sufficiently refined mesh to solve the flow gradients of interest across the wall boundary layer. The boundary layer region closest to the wall could be divided into three sublayers, with different flow characteristics in each of them. The sublayers are divided by a dimensionless wall distance parameter y^+. It is defined as

$$y^+ = \frac{y u_\tau}{\nu}$$

where y is the distance to the nearest wall, u_τ is the friction velocity at the nearest wall and ν is the local kinematic viscosity of the fluid. Table 2.1 and Figure 2.2 depicts how the three regions are divided with respect to the dimensionless wall distance y^+.

Table 2.1: The division of sublayers with respect to y^+.

Area		y^+	
Viscous sublayer	$0 <$	y^+	< 5
Buffer layer	$5 \leq$	y^+	≤ 30
Log layer	$30 <$	y^+	≤ 500
Outer region	$500 <$	y^+	

The shape of the curve depends on the relation with the dimensionless speed u^+, defined as

$$u^+ = \frac{u}{u_\tau}$$

where u is the velocity of the fluid parallel to the wall. Within the viscous sublayer, the curve increases linearly in relation to the dimensionless speed, $u^+ = y^+$.
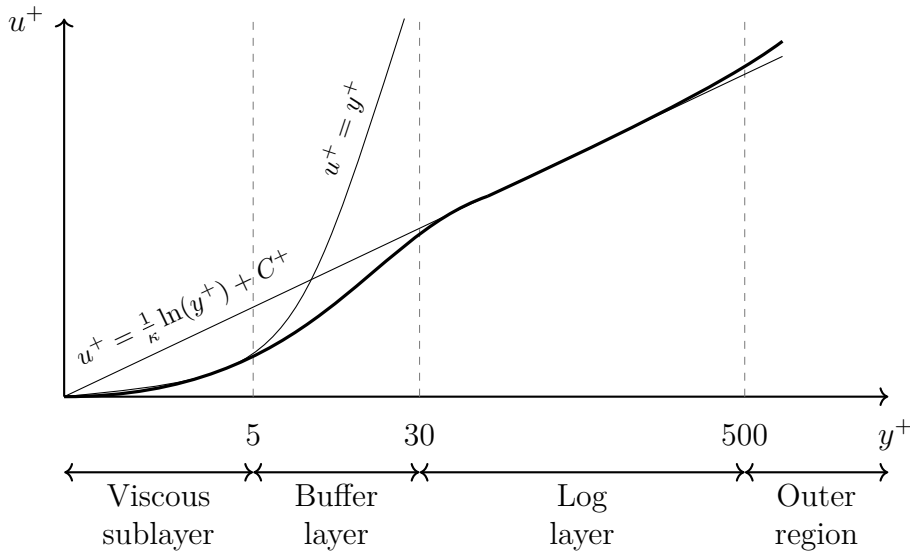
Figure 2.2: Relation between the dimensionless wall distance, y^+, and the dimensionless speed, u^+.

In the log layer, the curve increases logarithmic according to the law of the wall as $u^+ = \frac{1}{\kappa}\ln(y^+) + C^+$, where $\kappa \approx 0.41$ denotes the von Karman constant and the constant $C^+ \approx 5.0$ for smooth shapes [9][10].

2.3 Numerical methods

Numerical methods discussed in the report are explained below.

2.3.1 Algebraic multigrid

The Algebraic Multigrid (AMG) is a method working within Star-CCM+ to decrease the required computational time. This is done by solving the coarse-grid equations by using arithmetic combinations of the coefficients derived from the fine-grid equations. The grid levels are swept over by different cycle-techniques, where the V-cycle is the default and simplest method. The procedure is then started by some sweeps at the finer-grid levels, where the residuals then transfers all the way to the coarsest-grid level. After some sweeps at the coarsest level, the solution is transferred back to the finest-grid level where the solution is used to correct the next solution. The path of the cycle is then shaped as a V, explaining the name of the cycle. If the system is stiff, a W-cycle might be needed, where more iterations on the coarser-grid levels are performed in order to increase stability [11].

2.3.2 Cell quality remediation

The cell quality remediation identifies cells with low quality by measuring the skewness angle and other predefined criteria. The cells detected as poor-quality elements are then treated with gradients working to enhance the stability of the solution [12].

2.4   Multiphase flows

A flow consisting of more than one phase simultaneously in a domain of interest is referred to as a multiphase flow. The flow inside the ORVR system includes both liquid and vapourized fuel together with air and is hence a complex composition of material and phases.

2.4.1   Eulerian-eulerian

In multiphase flows, different approaches of how to solve the governing equations of the flow field are available. The Eulerian-Eulerian approach is commonly used because of its close relation to measuring techniques. Both the fluid and particle phase is treated as a continuum and the governing equations have a similar structure for all phases, which are solved simultaneously [13].

2.4.2   Volume of fluid

One way of modelling a multiphase flow of two fluid phases with non-negligible volume fractions is the Volume of Fluid method (VOF). The main idea is to model the interface between the phases on a stationary grid. By using a colour function the ratio of a certain phase in a computational cell is expressed as

$$\gamma = 1 \implies \text{only phase 1 in control volume}$$
$$\gamma = 0 \implies \text{only phase 2 in control volume}$$
$$0 < \gamma < 1 \implies \text{interface passing through control volume.}$$

The colour function is then passed into the governing equations which are written

$$\frac{\partial}{\partial t}\langle \rho_1 \rangle + \nabla \cdot \langle \rho_1 \mathbf{u}_1 \rangle = 0$$
$$\frac{\partial}{\partial t}\langle \rho_1 \mathbf{u}_1 \rangle + \nabla \cdot \langle \rho_1 \mathbf{u}_1 \mathbf{u}_1 \rangle = \nabla \cdot \langle \mathbf{T}_1 \rangle + \langle \rho_1 \mathbf{g} \rangle,$$

where $\mathbf{T}$ is the stress tensor and $\mathbf{u}$ is the velocity vector, for single phase flow and

$$\frac{\partial}{\partial t}\langle \gamma \rho_1 \rangle + \nabla \cdot \langle \gamma \rho_1 \mathbf{u}_1 \rangle = 0$$
$$\frac{\partial}{\partial t}\langle \gamma \rho_1 \mathbf{u}_1 \rangle + \nabla \cdot \langle \gamma \rho_1 \mathbf{u}_1 \mathbf{u}_1 \rangle = \nabla \cdot \langle \gamma \mathbf{T}_1 \rangle + \langle \gamma \rho_1 \mathbf{g} \rangle + \frac{1}{V} \int_{A_I} \mathbf{T}_1 \cdot \mathbf{n}_{I12} dA$$

for the first of two phases in multiphase flow. The last term in the momentum equation is the momentum transfer across the interface. Note that these are only equations for the first phase, the second phase is similar but γ is switched for $(1-\gamma)$ and the indices are 2 instead of 1.

The common density and stress is then expressed as

$$\rho = \langle \rho_1 \gamma + \rho_2 (1 - \gamma) \rangle$$
$$\mathbf{T} = \langle \mathbf{T}_1 \gamma + \mathbf{T}_2 (1 - \gamma) \rangle$$

and the final equations for VOF is then

$$\frac{\partial \rho}{\partial t} + \nabla \cdot (\rho \mathbf{u}) = 0$$

$$\frac{\partial}{\partial t}(\rho \mathbf{u}) + \nabla \cdot (\rho \mathbf{u}\mathbf{u}) = \nabla \cdot \mathbf{T} + \rho \mathbf{g} + \mathbf{F}_\sigma + \mathbf{F}_{\text{wall adhesion}}.$$

Here $\mathbf{F}_\sigma$ denote the surface tension force and the velocity is assumed continuous over the interface. The interface can then be tracked with Equation 2.8 [14]

$$\frac{\partial \gamma}{\partial t} + \nabla \cdot (\gamma \mathbf{u}) = 0. \tag{2.8}$$

The VOF scheme tends to be unstable for higher order schemes but suffers from numerical diffusion for lower order schemes. Therefore, advection schemes are used to provide a sharp interface and unambiguous profile of the colour function.

2.4.3 High resolution interface-capturing

The High Resolution Interface-Capturing (HRIC) scheme tracks the sharp interfaces between two immiscible phases. The scheme is based on the normalized variable diagram which calculates the normalized face value, ξ_f, as follows:

$$\xi_f = \begin{cases} \xi_c & \text{if} \quad \xi_c < 0 \\ 2\xi & \text{if} \quad 0 \leq \xi_c < 0.5 \\ 1 & \text{if} \quad 0.5 \leq \xi_c < 1 \\ \xi_c & \text{if} \quad 1 \leq \xi_c \end{cases}$$

The normalized face value is then further corrected based on the Courant number, calculated in Equation 2.5. This is to make sure that, during a time-step, the volume of a fluid that is moved over a cell face is not larger than what is available in the donor cell. This gives the expression:

$$\xi_f^* = \begin{cases} \xi_f & \text{if} \quad Co < Co_l \\ \xi_c + (\xi_f - \xi_c)\frac{Co_u - Co}{Co_u - Co_l} & \text{if} \quad Co_l \leq Co < Co_u \\ \xi_c & \text{if} \quad Co_u \leq Co \end{cases}$$

Here Co_l and Co_u are lower and upper limits and are by default set to 0.5 and 1, respectively. The above equation gives that for Courant numbers below the lower limit, the CFL condition is used. For values above the upper limit a first order upwind scheme is used, and between the limits a combination between the two is used. One more correction is done to account for the angle θ between the interface and cell-face.

$$\xi_f^{**} = \xi_f^*(\cos\theta)^{C_\theta} + \xi_c \left(1 - (\cos\theta)^{C_\theta}\right) \tag{2.9}$$

where C_θ is a constant set to 0.05. The equation for the cell-face value can then be written as:

$$\alpha_f^{\text{HRIC}} = \xi_f^{**}(\alpha_D - \alpha_U) + \alpha_U \tag{2.10}$$

where alpha with subscripts D, U, and f denotes the values at the downwind and upwind nodes as well as the cell-face, respectively [15].

2.4.4 Evaporation

Evaporation is a subcategory of vapourization that occurs when the temperature of the liquid is below its boiling point. The phenomenon occurs when molecules of a liquid have enough kinetic energy to escape the bonds of its neighbours. The opposite reaction is condensation, where the vapours condensates to liquid phase.

General evaporation consists of two stages: One, the transport of molecules from the surface of the liquid to the gaseous phase, and two, the diffusion of the evaporated molecules in the gaseous phase. The first phase is much harder to mathematically model. Therefore, most models make some assumption that the closest to the interface is saturated [16]. This is called hydrodynamic models, and is what is used in Star-CCM+.

2.4.4.1 Evaporation in Star-CCM+

In Star-CCM+ the evaporation and condensation model deals with the mass transfer between a gas and liquid phase over the free surface of the VOF model. It treats the phases as multicomponent mixtures and allows for non-interacting components, air for instance, in this case. The phases are handled as if in equilibrium, described by Raoult's law and driven by the diffusion of species.

The rate of evaporation for a material component i is described as

$$\dot{m}_i = -\frac{\rho_g D_{g,i} \left.\frac{\partial Y_{g,i}}{\partial \mathbf{n}}\right|_s}{1 - \sum_{j=1}^{N_v} Y_{g,j}^s} \tag{2.11}$$

where Y is the component mass fraction, D is the diffusion coefficient and N_v is the number of evaporating components. The subscript g denotes the gas phase and the superscript s denotes the surface.

The vapour pressure of a certain component i is described by

$$p_i = a_i p_i^*.$$

p_i^* is the vapour pressure of a pure component while a_i represents the activity that is determined by the liquid mixture. a_i is written as $a_i = \gamma_i X_{L,i}$. The activity coefficient γ is assumed to be $\gamma \approx 1$, which is stated in Raoult's law. The molar fractions at the interface is described by the relation between the vapour pressure, p_i, and the pressure, p, written as

$$X_{g,i}^s = \frac{p_i}{p}.$$

The vapour mass fraction at the surface is written as

$$Y_{g,i}^s = \frac{X_i^s W_i}{\sum_{j=1}^{N_v} X_j^s W_j + \sum_{j=1}^{N_{g,p}} X_j^s W_j}$$

13

where $N_{g,p}$ represents the number of non-interacting components in the gas phase and W_i is the molar weight of the components. The background molar weight, W_{bg} is calculated as

$$W_{bg} = \frac{\sum_{j=1}^{N_{g,p}} X_j W_j}{\sum_{j=1}^{N_{g,p}} X_j}$$

which acts as an approximation to calculate the molar fraction of the unknown non-interacting species. The background molar fraction at the face is calculated as

$$X_{bg}^s = 1 - \sum_{j=1}^{N_v} X_j^s,$$

which is used in order to approximate the interfacial vapour mass fraction, written in Equation 2.12.

$$Y_{g,i}^s \approx \frac{X_i^s W_i}{\sum_{j=1}^{N_v} X_j^s W_j + X_{bg}^s W_{bg}} \tag{2.12}$$

The liquid and gas volume fraction, α_l and α_g, is then used in order to define the total mass fraction for every component

$$Y_{g,m} = \alpha_l Y_{g,i}^s + \alpha_g Y_{g,i},$$

which is used in Equation 2.13, stating the approximated evaporation rate for one cell

$$\dot{M}_{i,c}' \approx -\frac{\rho_g D_{g,i} \nabla Y_{g,m} \nabla \alpha_l V_c}{1 - \sum_{j=1}^{N_v} Y_{g,j}^s}. \tag{2.13}$$

The transport of species towards and away from the interface of the phases is computationally expensive to model since it requires a sufficiently fine mesh to be captured accurately. This could be seen by comparing Equation 2.11 and Equation 2.13, where a lowest order analysis depicts that the relative error of the evaporation rate highly depends on the thickness of the boundary layer above the interface. The resolution of the mesh determines how accurate the location of the interface and boundary layer are modelled and therefore also how precise the evaporation rate is calculated [17].

2.4.4.2 Evaporation in GT-Suite

The evaporation in GT-Suite is defined as diffusion based mass transfer, called *Heat and mass transfer*. The mass balance for the phases are then defined as

$$\frac{dm_g}{dt} = +\dot{m}_{\text{evap}} - \dot{m}_{\text{cond}}$$

and

$$\frac{dm_l}{dt} = -\dot{m}_{\text{evap}} + \dot{m}_{\text{cond}}$$

for the gas and liquid phases, respectively. By calculating an array of mass fractions based on Raoult's law in the system, f_l, the mass transfer rate of the liquid to gaseous phase can be written as

$$\dot{m}_{evap} = \frac{df_l}{dt} \times m_l$$

where m_l represents the mass of the liquid phase [18].

2.4.4.3 Implementation of the evaporation model into the governing equations

The evaporative mass transfer between the phases can be included in the governing equations using an additional scalar field. Both fluids are assumed incompressible, giving the momentum conservation equation as

$$\rho \left(\frac{\partial \boldsymbol{u}}{\partial t} + (\boldsymbol{u} \cdot \nabla)\boldsymbol{u} \right) = -\nabla p + \nabla \cdot \tau + \sigma \kappa \nabla \alpha + \boldsymbol{f}$$

with the viscous stress tensor defined by

$$\tau_{ij} = \mu \left(\frac{\partial u_i}{\partial x_j} + \frac{\partial u_j}{\partial x_i} \right),$$

while $\boldsymbol{u}$ and p represents the velocity and pressure fields. The surface tension, σ, is assumed constant. The liquid volume fraction is denoted α, which is assumed either 1 or 0 since a sharp interface between the vapour and liquid is assumed. The curvature of the interface is represented by κ, which is expressed as

$$\kappa = -\nabla \cdot \frac{\nabla \alpha}{|\nabla \alpha|}.$$

The body forces are all collected in $\boldsymbol{f}$.

The mass conservation equation is written as

$$\rho \nabla \cdot \boldsymbol{u} = \dot{\rho},$$

where $\dot{\rho}$ is a source-term described later on. The enthalpy equation is expressed as

$$\frac{\partial}{\partial t}(\rho c_p T) + \nabla \cdot (\rho c_p \boldsymbol{u} T) = \nabla \cdot (\lambda \nabla T) + \dot{h},$$

with T as the temperature, c_p the specific heat capacity and λ the thermal conductivity. Physical heat sources may be contained in the source term $\dot{h}$, together with the contribution of the enthalphy of evaporation. The source term $\dot{\rho}$ is chosen such that in the liquid side of the interface between the phases, mass disappears and reappears on the vapor side.

The gradient of the volume-fraction field is computed as

$$\alpha' = |\nabla \alpha|.$$

The integral of the volume-fraction α' over a region enclosing a part of the vapour-liquid interface measures the interface, meaning that the three-dimensional volume integral gives the interface area and in two dimensions the corresponding area integral gives the interface length. This is used in the evaporation model in Star-CCM+, since the integral of the gradient of the liquid volume-fraction, $|\nabla\alpha|$, over a certain volume expresses the area of the interface it contains, and hence the evaporation rate $\dot{M}'_{i,c}$ for one cell can be obtained, seen in Equation 2.13 [17][19].

2.4.5 Antoine's equation

The saturation pressure could be calculated by Antoine's Equation, which is written as Equation 2.14

$$\log_n\left(\frac{P_{sat}}{P_{atm}}\right) = A - \frac{B}{T + C} \tag{2.14}$$

where the base could be either e or 10, P_{atm} is 1 bar and the temperature T is in Kelvin. The constants A, B and C are fluid specific coefficients.

2.4.6 Gasoline

Gasoline is a commonly used fuel in automobiles. It is extracted from crude oil and contains a wide variety of components. These components have varying vapour pressures implying that the rate of evaporation varies between them. The consequence of this could be that the evaporation rate, in constant ambient conditions, varies with time, as some components are more or less depleted. It also means that all of the gasoline will not evaporate given a very long time, since some components do not evaporate at all.

There is also a number of variations of gasoline available. These vary with geographical location and season. The main difference is a variance in vapour pressure. In regions with colder temperatures, a higher vapour pressure is required to achieve combustion, and in hotter regions a lower vapour pressure keeps the emissions down [20].

In the simulations done for this thesis the gasoline is assumed to consist of only one component. This is a valid assumption since simulations can only be done for a relatively short amount of time, roughly a number of seconds. The effects of the many components previously discussed does therefore not come into play. In the simulations a gasoline variation called *EPA Tier 3* is tried to be mimicked. That is one of the types of fuels used in ORVR measurements for certification towards the US market.

2.5 Literature survey

A literature survey of earlier works and stability treating evaporation was performed and what follows is the main points from those.

2.5.1 Thesis at fuel system department 2019

During the spring of 2019 Anton Ringström and Aditya Naronikar performed a thesis work on the refuelling system at Volvo cars. They did three-dimensional simulations in Star-CCM+ and performed physical experiments of the ORVR system. These results were then compared. The simulation setup lacked a model for evaporation of the fuel, which created the need of this project. The used CAD-files of the system in Star-CCM+ were also used during this project and the mesh was constructed in a similar way, but with a refined region around the surface of the fuel in the tank and an independent mesh study, see Section 3.1.3.1. The thesis can be read at [1].

2.5.2 Enhancing stability of evaporation in simulations

The literature treating the evaporation model in Star-CCM+ is rather short, especially the information about how the model works to enhance stability of the solver. Other sources dealing with evaporation models implemented in various softwares were therefore studied to get an extended understanding of the stability issue of the evaporating phenomena in multiphase problems.

One possible source of instability is the coupling between the droplets and flow equations, since they typically are solved at different time scales. The droplets are traditionally treated with a Lagrangian approach while the gas phase is treated with an Eulerian approach. The equations treating the evaporation of droplets are then typically treated with a time step around 10^{-6}, while the global time step for the gas phase typically are solved with a time step around 10^{-4}. This situation are especially appearing when the system of ordinary differential equations treating the droplet dynamics is stiff, since the coupling between the phases are affected by the different time scales. This problem can be managed by the decomposition of the systems into simpler subsystems, which is commonly implemented in engineering applications [16].

The convective and diffusive transport equations are limited on different ways, where the fuel flow in this study is stabilized by the CFL condition, while the vapours instead are limited by the diffusive stability constraint written as

$$\frac{2D_{vg}\Delta t}{\Delta x^2} \leq 1$$

where D_{vg} represents the binary diffusion coefficient of the vapour inside the gas, Δt the time step and Δx the length of the computational element [21]. The difference between those limiting constraints may be a reason for instability in the solver.

3

Method

The following chapter describes the methodology used during the study. It contains the setups of the performed simulations, the procedure of validating the evaporation model and the procedure for an alternative one-dimensional simulation.

3.1 Simulation setup

The main simulations of the refuelling process in the ORVR system were performed in the CFD solver Star-CCM+, version 2020.1. An existing CAD model of the fuel tank was used as computational domain in the simulations. Since a fuel tank is complex with many small details, the model had been cleaned up beforehand, meaning that small details considered indecisive for the fuel flow were removed to decrease the computational effort during the simulations.

3.1.1 Boundary conditions

During the first 0.1 seconds, the velocity of the fuel inflow increases linearly until it reaches its constant velocity of 38 l/min. This corresponds to the velocity of a regular fuel flow injection during refuelling.

The temperature in all regions was set to 20°C and the walls were assumed adiabatic. The hydrostatic pressure from the fuel in the tank was defined as dependent on the height of the liquid. Since the canister was not modelled in the simulations, it was replaced by a pressure drop from the outlet of the LCO. This pressure drop was interpreted as a porous wall and it's values were calculated with the use of material properties and data provided from the company.

The initial height of the fuel in the tank was varied between a pre-fill of approximately 10%, and a height just before the fuel tips over to the space between the active and the passive side of the tank. The mass fraction of gasoline vapour and air of the gaseous phase in the tank was initially defined as 60% gasoline vapour and 40% air. This was done because of the ratio of the gases when in equilibrium, obtained from an experimental simulation later described in Section 3.3.2. The mass fraction of gasoline vapour in the filler pipe was set to 0%, which implies pure air, when the refuelling was done with the low pre-fill in the tank.

3.1.1.1 Measurement of saturation pressure

The saturation pressure of the EPA Tier 3 was experimentally measured using a machine called MiniVap VPXpert made by Grabner Instruments [22], shown in Figure 3.1.

Figure 3.1: Machine used to measure the saturation pressure of the used fuel.

This was done for 3 different temperatures; 17.8°C, 27.8°C and 37.8°C in order to be able to solve the material constants in the Antoine Equation of the saturation pressure. The measurement showed that the fuel had a saturation pressure of approximately 33kPa at 20°C.

3.1.2 Solver settings

It is important to select the specific settings for the studied flow case in Star CCM+ to mimic the real-life conditions of the refuelling process. The selected physics in the simulation setup are listed in Table 3.1.

The selected models related to the Adaptive Time Step were the *Convective CFL Condition* and the *Free Surface CFL Condition*. The Convective CFL Condition changes the time step with respect to the CFL number, so that the time step becomes the smallest alternative of either the specified maximum CFL number or the specified mean CFL number. The maximum CFL number was set to 10.0 and the mean CFL number to 0.5. The Free Surface CFL Condition is suitable for flows with changing velocity field and when the VOF interface crosses meshes of varying refinement, such as the studied flow case. The time step is then limited to allow for a sharp interface with respect to the CFL number, weighted by the rate of change of volume fraction [23][24].

In order to catch the interface between the fuel and gas consisting of air and evaporated fuel in the tank, the Eulerian Multiphase Model was set to Volume of Fluid (VOF) with a VOF-VOF phase interaction. The primary phase was selected to be

gasoline while air was the secondary phase.

The $k - \epsilon$ Turbulence model is a suitable choice for the studied flow case, since it generates a good balance between stability, computational effort and accuracy [25].

Table 3.1: Physics models used in Star-CCM+.

Adaptive Time Step
Eulerian Multiphase
Gradients
Gravity
Implicit Unsteady
K-Epsilon Turbulence
Multiphase Equation of State
Multiphase Interaction
Realizable K-Epsilon Two-Layer
Reynolds-Averaged Navier-Stokes
Segregated Flow
Segregated Multiphase Temperature
Solution Interpolation
Three Dimensional
Turbulent
Two-Layer All y+ Wall Treatment
Volume of Fluid (VOF)
Wall Distance

The Two-Layer All $y+$ Wall Treatment was selected due to the complexity of the geometry and the mesh, where low-$y+$ wall treatment is used for fine meshes and the high-$y+$ wall treatment for coarse meshes within the boundary layer. When the wall-cell centroid is in between the viscous sub-layer and the log-layer, which implies the buffer region, the model is formulated to produce reasonable calculations which makes the model suitable for varying kind of near-wall mesh densities. The two-layer approach includes values for the turbulent dissipation rate, ϵ, which are applied at the centroids of the near-wall cells in order to correlate with the two-layer formulation of the turbulence model [26].

3.1.3 Meshing strategy

The geometric domain of the ORVR system is discretized into a cluster of computational cells, in which the flow structures are solved for in Star-CCM+. The volumetric mesh was conducted using a polyhedral mesh structure, since it requires less elements and are able to compute faster than a tetrahedral mesh without decreasing the accuracy of the solution [27]. The surface remesher model was activated at some parts to remesh the intial surface of the geometries. The initial surface is made of triangulated surfaces, which may contain highly skewed traingles. The surface remesher improves the quality of the surface mesh by generating evenly-sized

triangles which decreases the skewness of the triangles [28].

The mesh was done by parts-based automated meshing. The surface and volumetric controls were all set to depend on the base size of the mesh, meaning that all parts were refined in a correlating way when reducing the overall base size of the automated mesh.

The filler pipe was regarded a critical region for the fuel flow and by that a volumetric refinement region was created within the part, with an element size of 10% of the base size. The surface of the fuel in the tank and the region where the fuel enters the tank was also regarded important to model accurately, why a surface remesher was activated in both volumetric refinements and an element size of 20% and 55% of the base size, respectively. For the case where the fuel flows over from the active to the passive side of the tank, refinement boxes were activated at the slope and at the bottom of the passive side, where the flow entered. The placement of the refinement boxes in the tank for the top- and low-fill cases are shown in Figure 3.2. The blue boxes represents the placement of the refinement boxes treating the low-fill case while the green boxes are active for the top-fill case.
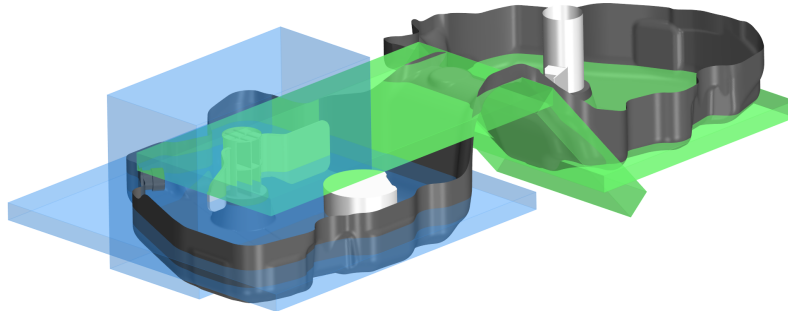
Figure 3.2: Placement of refinement boxes in the tank, where the blue boxes represents the refinement boxes for the low-fill case and the green boxes the top-fill case.

The fuel pistol, where the gasoline was injected, had both a surface remesher and a prism layer mesher activated in the volumetric refinement. The element size was set to 15% of the base size and 3 prism layers with a total thickness of 15% of the base size in order to maintain the y^+ values within the log layer region. Due to small cross section areas in the recirculation line and LCO box outlet, the mesh was made finer and by that the y^+ became less than 5 in those regions, why the Two-Layer All y^+ wall treatment was a suitable model.

3.1.3.1 Mesh dependency study

To try to ensure that the simulations were converged, a mesh dependence study was performed. The reason behind this is both to verify that the results are trustworthy,

but also to create an effective simulation setup. The aim is to produce a mesh which generates sufficiently accurate results while keeping the required computational time as low as possible. The study only treated the low-fill case, meaning that the top-fill case was not evaluated.

The procedure started by generating a mesh which was assumed very fine, which would by that generate reliable results from a meshing point of view. Based on this mesh, a criterion of around 5% margin of error was decided to be sufficiently accurate. The finest mesh evaluated during this study had a base size of 6.0mm which gave a mesh consisting of approximately 10 millions of elements. This was regarded a reasonable amount of cells for being sufficiently fine at the time for the mesh dependency study. The flow time was set to 3 seconds, which was approximated to be a suitable time since the fuel flow would then be fully developed into the tank and the measured values then should become stable. The evaluated quantities in the mesh dependency study are listed below:

- The mass flow rate through the LCO outlet, time averaged over the last second of flow time.
- Surface averaged static pressures at different cross sections along the length of the filler pipe, time averaged over the last second of flow time.
- The time averaged value of the pressure drop along the recirculation line over the last second of flow time.
- The static pressure in the tank calculated as the average surface pressure on the FDM cap, time averaged over the last second of flow time.
- The overall volume avegared evaporation rate in the entire domain, time averaged over the last second of flow time.

Three different meshes were investigated during the mesh study, where all parameters of the studied meshes were set as dependent on the base size. The details of those are shown in Table 3.2.

Table 3.2: Data of the investigate meshes in the mesh dependency study.

	Fine mesh	Coarser mesh	Adaptive mesh
Base Size	6.0	7.0	48.0
Number of cells	10 millions	7 millions	Adaptive - around $2-3$ millions

The adaptive mesh is a feature that refines or coarsens cells during the simulation based on the current situation. The models used in the mesh dependency study were the free surface mesh refinement with a max refinement level of 2. The free surface refinement model works as a part of the VOF model to refine the free surface between the gas and liquid phases [29]. The aim of using an adaptive mesh is to not use more cells than needed to get an accurate solution. It uses automatic refinement in areas where it is needed. This could then save important computational time. The reason for the high base size of the adaptive mesh was that the adaptive mesh model was a brand new feature when the mesh dependency study was made, while

the need of saving computational time was high. The expectations of the adaptive mesh were high in advance, but a further investigation of a suitable base size when using the adaptive mesh model was afterwards discovered to be a suitable further development of the mesh dependency study, which would have been done if more time was available. The result of the mesh dependency study can be found in Section 4.1.

3.2 Implementation of evaporation

The materials in the Eulerian Multiphase model were selected to multicomponent liquid and multicomponent gas. The liquid was then assumed incompressible and non-reacting, while the gas was assumed a non-reacting ideal gas. With this done, a sub-model called *Evaporation/Condensation* was selectable under the Multiphase Interaction module in Star-CCM+. How this model approximates the evaporation is further described in Section 2.4.4. The connectivity of the fuel and vapourized fuel were then coupled in the solver to define the mass transfer between the phases. All the models selected in the Multiphase Interaction module are depicted in Table 3.3.

Table 3.3: Phase interaction models used in Star-CCM+.

Evaporation/Condensation
Interface Momentum Dissipation
Multiphase Material
Surface Tension Force
VOF-VOF Phase Interaction

The surface tension of the gasoline was set to 0.022 N/m [30]. The interface momentum dissipation model adds extra momentum dissipation in the presence of the free surface to dissipate parasitic currents, caused by discretization errors due to discontinuities along the free surface. Those discretization errors might not scale with the mesh size, which is why the interface momentum dissipation is used to reduce the parasitic currents along the interface [31].

3.2.1 Trial-and-error workflow

The implementation of a working evaporation model in the simulation setup was the most time consuming part of the project. The combination of the relatively complex geometry and the evaporating phenomena of gasoline proved to be hard to manage. The aim was to mimic the real refuelling process as much as possible, which included the use of the measured saturation pressure, the measured mass fraction of vapourized fuel in the air in the tank and all other boundary conditions of the real ORVR procedure. Table 3.4 shows some of the tested changes to the simulation setup in order to generate a working simulation.

Table 3.4: The main trial-and-error workflow when implementing evaporation. Improved outcome implies that more iterations were possible to run before crash.

Default setting and test	Outcome
Default: Constant saturation pressure. Test: Saturation pressure to depend on Antoine's equation. *- The saturation pressure is able to change according the temperature when being dependent on Antoine's equation.*	Improvement
Default: 60% vapourized fuel in the air as initial condition Test: 0% vapourized fuel in the air as initial condition *- The lower mass fraction of vapours proved to stabilize the simulation in an early stage.*	Improvement
Default: Second order temporal discretization solver Test: First order temporal discretization solver *- First order increases the stability, but it might give some minor loss in numerical accuracy.*	Improvement
Default: AMG (Algebraic Multigrid) linear solver of pressure using V Cycle Test: AMG linear solver of pressure using W Cycle *- A W-cycle could stabilize a stiff system by increasing the iterations on the coarser-grid level.*	No Improvement
Default: No surface tension force Test: Addition of surface tension force *- A surface tension force enhanced the stability and mimics the reality.*	Improvement
Default: No cell quality remediation model Test: Addition of cell quality remediation model *- Poor-quality cells could be treated with gradients working to enhance the stability of the solution.*	No Improvement
Default: Maximum CFL number at 10 Test: Maximum CFL number at 5 *- Keeping the allowed maximum CFL-number low could decrease the time step, which could stabilize the solution.*	No Improvement

Default: Inflow velocity of 38 l/min Test: Lowering the inflow velocity to 15 l/min *- A lower inflow velocity could slow down all the processes, which might increase stability.*	No Improvement
Default: Mesh with approximately 10 million cells Test: Refine the mesh to double number of cells *- A refined mesh could possibly resolve the flow phenomena even more, which could increase stability.*	No Improvement
Default: Mesh with approximately 10 million cells Test: Run script showing bad cells, remove them *- A script delivered from the Star-CCM+-support detecting bad cells in the mesh was run, where the bad cells were then treated to enhance stability.*	No Improvement
Default: Standard relaxation factors Test: Decrease relaxation factors *- A lower relaxation factor implies a shorter step in the numerical solution method, which could increase stability.*	Improvement
Default: No linear ramp in the solver settings Test: Linear ramp of segregated flow the first iterations *- A linear ramp implements a low relaxation factor for a specified amount of iterations.*	No Improvement
Default: 8 inner iterations Test: Increase number of inner iterations *- An increased amount of iterations within every time step could increase the stability.*	No Improvement
Default: Saturation pressure as measured values Test: Saturation pressure as default gasoline values *- The default settings of the gasoline saturation pressure were able to run.*	**Big Improvement**

After weeks of trial-and-errors combined with consultation with the support team at Star-CCM+, it was decided that the saturation pressure had to be limited to be the default settings for gasoline while the mass fraction of vapourized fuel in the air had to be approximated to be 0%, meaning 100% clean air before the refuelling begins. More time was required to find and evaluate a working simulation setup with the measured saturation pressure of the EPA Tier 3 fuel.

3.3 Validation of implementation

To check that the evaporation model was implemented in a correct way, an experimental study was carried out. The test measured the evaporation rate of the EPA Tier 3 fuel, which corresponds to the fuel used when certifying to the American market. The fuel was put in a beaker with a small outlet opening on top. The experimental setup was then simulated in Star-CCM+ and GT-Suite and the results were compared to validate the accuracy of the evaporation model.

3.3.1 Experimental setup

The physical experimental study was done in a glass beaker with a total volume of 2000ml and an inside diameter of 150mm.
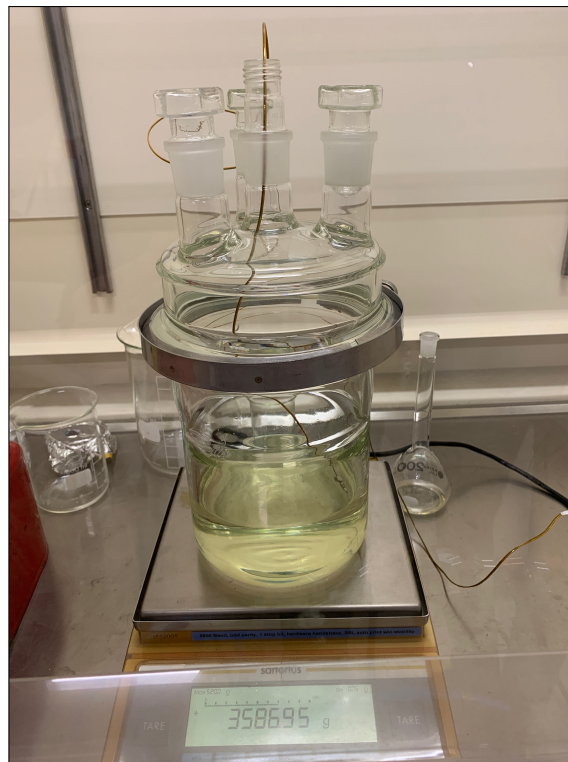
Figure 3.3: The beaker used in the experiment. On the lid there are four openings which are all closed, except for the one in the center.

On top a lid with a small central opening was placed to limit the outlet cross section area. The diameter of the lid opening was 12mm. The beaker was filled with roughly 700g of EPA Tier 3 fuel and placed in a chamber with room temperature. The test duration was 70 minutes, but the first minutes were deleted from the measured data because of changes of the experimental setup which may affect the results. The beaker was placed on a weighing scale and the weight was measured every minute to get the variation of evaporation and change in volume and mass over time. The temperature was also measured every minute to ensure that the environmental

condition remained the same. In Figure 3.3, a picture of the experimental setup is shown.

Volume Fraction of Gasoline
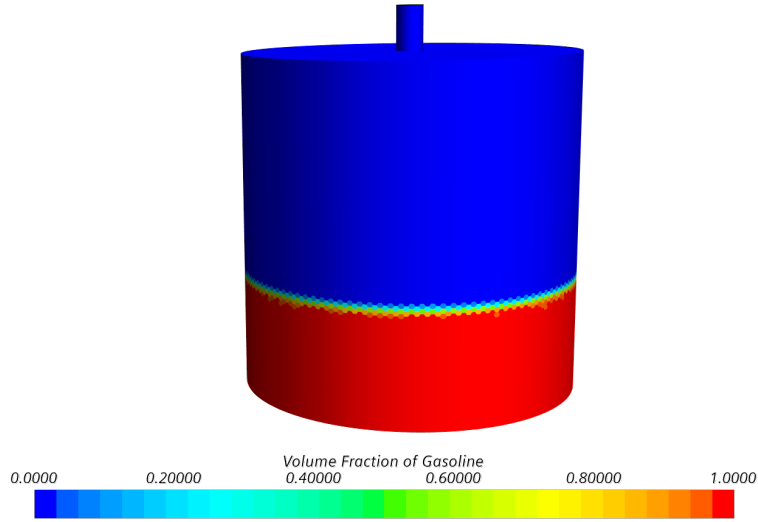
Figure 3.4: The geometry of the simulation setup. The figure shows the volume fraction of gasoline in the domain, giving a feeling for the location of the fuel.

3.3.2 Simulation setup

The simulation setup was created to mimic that of the experimental setup. The beaker diameter was set to 150mm and the outlet diameter was set to 12mm. The fuel was set to gasoline in the simulation, where the density and saturation pressure were set according to that of the EPA Tier 3 fuel. A picture of the simulation setup is depicted in Figure 3.4.

The same solver settings and physics models as in the ORVR simulation, previously shown in Table 3.1, were used. The saturation pressure was set as both the measured values of EPA Tier 3 in order to compare the evaporation rate with the experiment described in Section 3.3.1, but also as the default settings for gasoline in order to evaluate how much the evaporation differ in the simulations compared to the reality. The meshing strategy included a polyhedral mesh with the same settings for both simulations, with a base size of 2.1mm and a total of approximately 325000 cells. The maximum time step was set to 0.001s with an adaptive time step activated with a target mean CFL number at 0.3 and a target maximum CFL number at 3.0 in order to keep the time step sufficiently low to reach convergence.

3.4 One-dimensional setup

To further compare and evaluate the simulated results, a one-dimensional simulation was created. This was mainly done in the software GT-Suite, made by Gamma Technologies. It is important to consider the limitations of a one-dimensional simulation compared to a three-dimensional, crucial flow behaviour may be disregarded.

3.4.1 CAD pre-process

The studied components in GT-Suite of the ORVR-system was imported from a CAD-model featuring a Volvo XC90, the same car as previously studied in Star-CCM+. All components except from the fuel tank had to be modified in ANSA in order to remove unnecessary parts and to only consider the inner diameter of the pipes. The number of nodes of each component was also specified to get rid of sharp edges of the geometries.

After pre-processing the components in ANSA, they were imported into GT Space-Claim. The aim was to generate closed bodies of the geometries. It was done by use of the inbuilt repair tool in GT SpaceClaim. It closes the small openings in the surface that are normally a part of any CAD file. This tool did not always function perfectly, then manual intervention was required. Some parts of the pipes, and the other structures, have therefore completely been reconstructed.

3.4.2 CAD to one-dimensional conversion

The last step of the pre-process was to import the closed geometries into GEM3D, where the discretization from a three-dimensional CAD file into a one-dimensional setup was made.
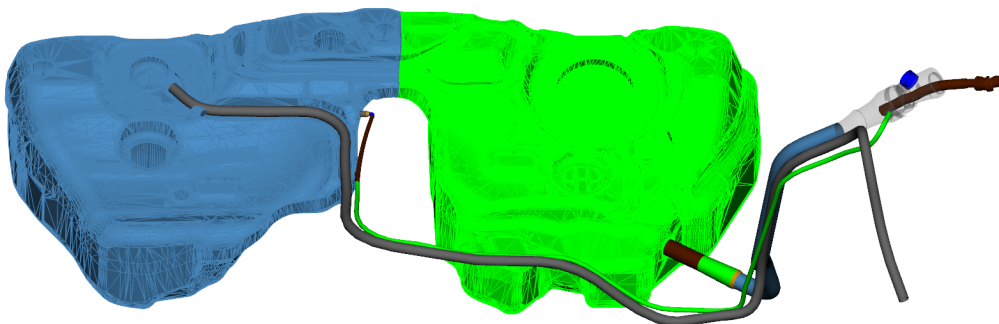
Figure 3.5: The full ORVR system implemented in GEM3D.

3.4.2.1 Tank in GEM 3D

The full ORVR system implemented into the software GEM3D is shown in Figure 3.5. The tank is divided into two parts, represented by the two different colors in the picture. It was split in half to account for the complex geometry of the tank. Since the initial conditions for the refuelling test required a 10% pre-fill, the split allowed for the pre-filled fuel to be positioned in the active side only.

3.4.2.2 Capless filler neck and filler pistol

The capless filler neck implemented into GEM3D is shown in Figure 3.6. Note the shape of the fuel pistol, which has a varying cross section area. The complex

geometry inside the fuel pistol used in the three-dimensional simulations was difficult to discretize. Instead it was replaced by a pipe with varying cross section area that approximates the active cross sectional area of the real pistol along its length. The capless filler neck was then discretized into smaller elements using a model called *Shell*. The model calculates the volume of the part and creates connections to intruding parts. The size of discretization elements were later chosen to roughly capture the shape of the filler neck. Figure 3.7 gives a view of the discretization, where each cube represents a computational element in GT-Suite. If the size of the cubes were to be reduced, the numbers of elements would increase which could possibly increase the computational accuracy in the filler neck. At the same time it would also require more computational time to simulate as well as a longer set up time, as elements have to be set up individually.

3.4.2.3 Air inlet

The air inlet was moved from its original position in order to allow the discretization to be made. On the real system the air inlet is the same opening as the one the filler pistol is entered into. It was found that the co-axial position of the inlet and filler pistol was difficult to implement. Therefore the intake was instead moved on top of the filer neck and can be seen in Figure 3.6 and 3.7. The area is calculated as to be the same as that of the real inlet with the filler pistol inserted.

3.4.2.4 Filler pipe

The geometry of filler pipe, going from the capless filler neck to the opening of the fuel tank, was implemented into GEM3D with the geometry shown in Figure 3.8. The model used to discretize the pipe had difficulties handling a varying pipe diameter. One part's diameter could either constantly increase or decrease. Therefore, the pipe is split into four parts, capturing the shape better.
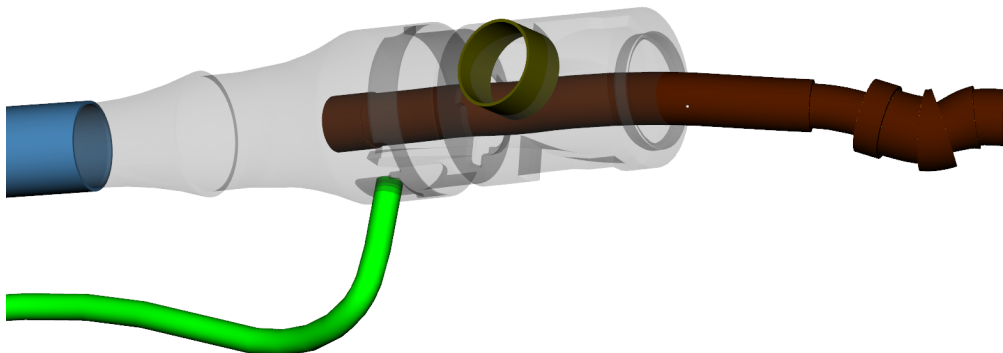
Figure 3.6: The filler neck with all neighbouring parts. To the left the filler pipe is connected, to the right the filler pistol, on top the air inlet and to the bottom of the picture the recirculation pipe.
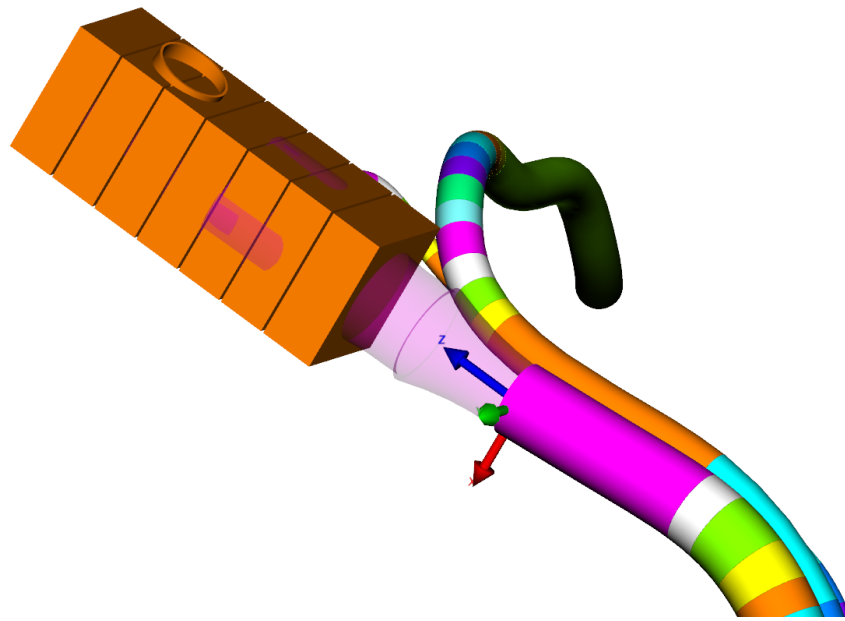
Figure 3.7: The discretization visualization of the capless filler neck. A cube represents one element in the GT-Suite file, see Figure 3.10.
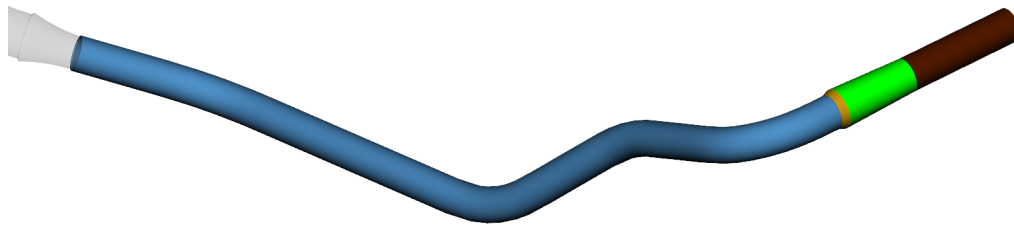
Figure 3.8: The filler pipe connected to the filler neck to the left and the tank to the right.

3.4.2.5 Recirculation pipe

The end of the recirculation pipe implemented into GEM3D are depicted in Figure 3.9. Similarly to the filler pipe the recirculation pipe was split into several parts, in this case five. This was done both because of the varying diameter and the sharp bend at the end towards the tank, as is seen in the figure. Most of the pipe was still one section with a constant diameter stretching up to the filler neck. This long part is the green pipe and can be seen both in this figure as well as in Figure 3.5 and 3.6.

Figure 3.9: The end of the recirculation pipe that is fitted to the opening in the tank. The green part extends all the way up to the filler neck, as can be seen in figure 3.5.

3.4.3 EVAP line

In Figure 3.5 the EVAP line can be seen. It goes from the LCO outlet at the tank to the canister, which is located somewhere close to the filler neck. In the figure it is colored gray and is not split into several parts.

3.4.4 Simulation setup
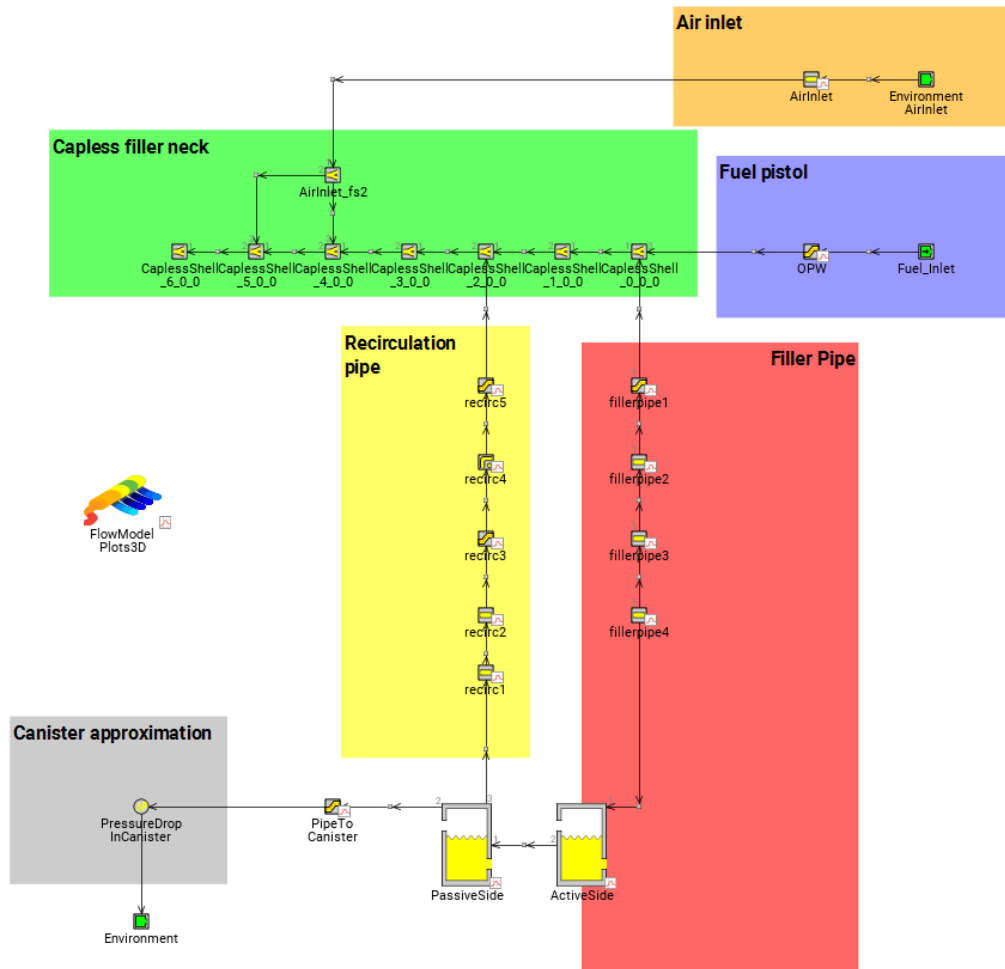
Figure 3.10: The full ORVR system implemented in GT-Suite.

The full ORVR system implemented in GT-Suite is shown in Figure 3.10. It displays all parts visible in Figure 3.5 in one-dimensional form. Also a pressure drop, used as an approximation for the canister, hereafter called canister pressure drop, is included in the bottom left connected to an atmosphere outlet. The big blue rectangle is the capless filler neck. Each element inside of it corresponds to one cube in Figure 3.7. The filler neck is connected to the air inlet and filler pistol. They are then connected to the atmosphere and a velocity inlet boundary condition, respectively. The filler neck is also connected to the filler pipe and recirculation pipe, each containing four and five elements, respectively. The filler pipe is then attached to the active side of the tank and the recirculation pipe to the passive side. From the passive side the

EVAP line goes to the canister pressure drop.

An implicit time integration scheme was selected with a time step size of 0.001 seconds, which gave converging simulations. The phase transfer was set to Heat and mass transfer with a saturation pressure of 33kPa. Initially the system is filled with air, except for the active side of the tank and the filler pipe. The active side of the tank is initially filled with 7.1 liters of fuel, 10% of the tank volume. The filler pipe was also filled with fuel initially. This remedy is mainly to solve a problem where the fuel starts to exit through the air inlet instead of entering the tank. The first five seconds of the simulation the system is at rest. This means that during the first five seconds there is no inflow through the fuel pistol, which minimizes errors during the initial stage with the system reaching a pressure equilibrium and the first vapour development. Then, after five seconds, the refuelling begins. The refuelling stops when the tank is filled, at approximately 95% of the nominal volume. The gas phase consisted of 100% air, like the three-dimensional setup.

3.4.5   Variation of setups

A number of different setups were tried during the development of the one dimensional systems. Two different tank models, called Tank3D and FluidReservoir, and a number of different discretizations of the filler neck.

The Tank3D model uses a CAD file to specify the geometry of the tank. This means that flow properties such as passive side overflow is captured. This model does however have stability issues when handling evaporation, and as such was not perfect for this problem.

The FluidReservoir model approximates the tank geometry as a cylinder. The geometry can however be further specified with relations of liquid surface area, height and volume. This model handles evaporation better than the Tank3D model and when the tank was split into two parts a sufficient part of the flow behaviour was captured. Therefore, the FluidReservoir was chosen as the main used model, but the Tank3D model will also be compared to it.

Some different discretizations of the capless filler neck were also tried. Three variations were tried. First, a single element for the entire filler neck was tried, but it resulted in nonphysical behaviours. The other two models used were finer. One with slices along the axis of the filler neck and can be seen in Figure 3.7 and belonging system in Figure 3.10. This discretization was the one used in the main simulation setup, which results will be discussed. The other even finer separated into cubes to further capture the shape of the part, it can be seen in Figure A.2 with the belonging system in Figure A.3, both can be found in the appendix.

4

Results and discussion

The following chapter contains the results from the simulations and experimental studies. The main one-dimensional results shown are from the FluidReservoir model. Only the low-fill case is investigated in the three-dimensional simulation since this pre-fill level contains more possible comparisons than the top-fill case, because of time limitations. The results are normalized implying that only the relation between the results will be evaluated. The results of the mesh dependency study are normalized towards the finest mesh investigated, the results of the pressure in the tank are normalized towards experimental data and in the other cases the results are normalized towards the three-dimensional simulation with evaporation activated.

4.1   Mesh dependency study

The base size of the adaptive mesh used in this mesh dependency study might have been to high, which is a possible explanation why the results from the adaptive mesh were far off the measured results from the other meshes, which will be seen in the following figures.

The first measured results were the mass flow rate through the outlet of the tank, going towards the carbon canister, at the LCO outlet. The mass flow rate of the three investigated meshes are shown in Figure 4.1.
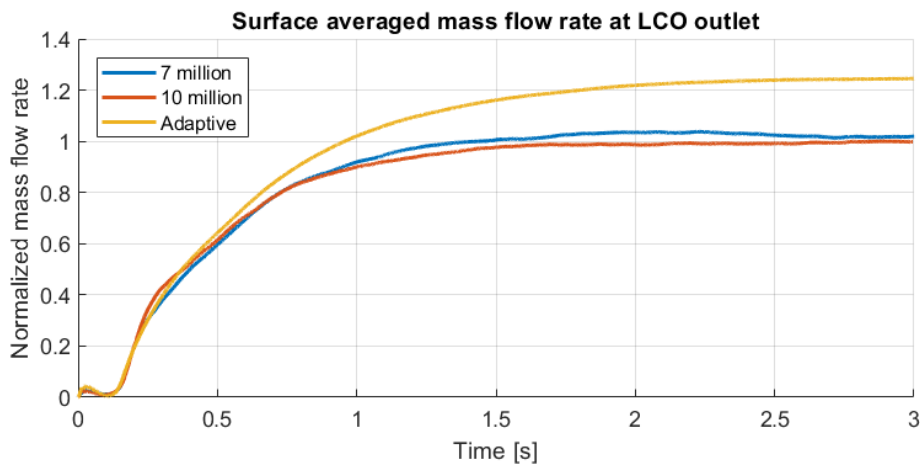
Figure 4.1: Surface averaged mass flow rate at the LCO-outlet for the investigated meshes.

When time averaging the values over the last second of flow time, the coarser mesh with 7 million cells are 3.2% higher than the results of the fine mesh. As earlier discussed, the results from the adaptive mesh are far from the fine mesh and not suitable to further evaluate. The results from the adaptive mesh are far off in all studied parameters, which is why it will not be discussed in detail during the further comparison within the mesh dependency study.

The pressure along the filler pipe was evaluated as a surface average on 4 different locations spread along the filler pipe. The time averaged results of this over the last second of flow time are depicted in Figure 4.2. As can be seen, there are small differences between the fine and coarser meshes, while the adaptive mesh is generating inaccurate results.
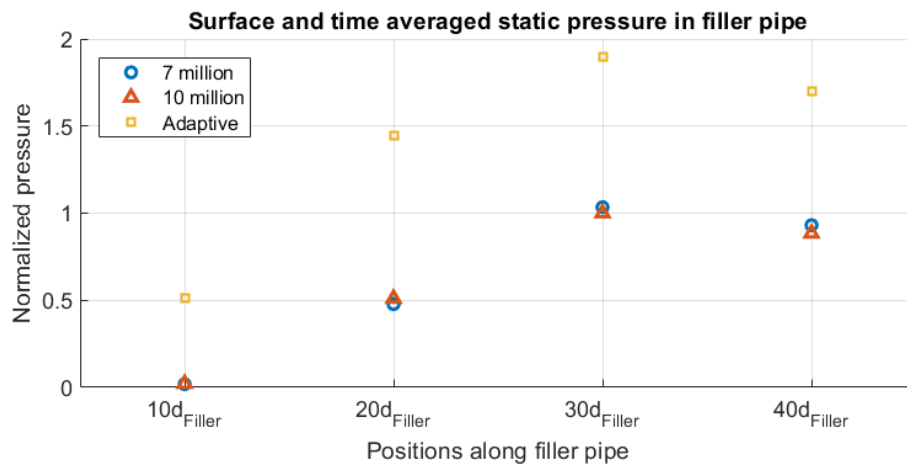
Figure 4.2: The figure shows the normalized pressure at different locations along the filler pipe. The pressure is time averaged over the last simulated second.
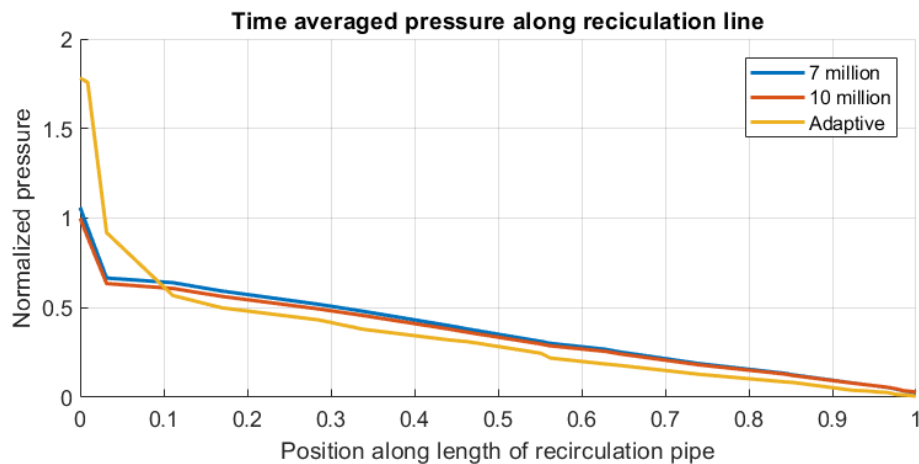
Figure 4.3: The variation of pressure along the length of the recirculation pipe. The values are time averaged over the last simulated second.

In the same way, the pressure along the recirculation line was evaluated as time averaged values over the last second of flow time along the length of the pipe, seen in

Figure 4.3. The differences between the meshes are small. The time averaged values over the last second of flow time indicates a difference of around 5.1% between the fine and coarser meshes.
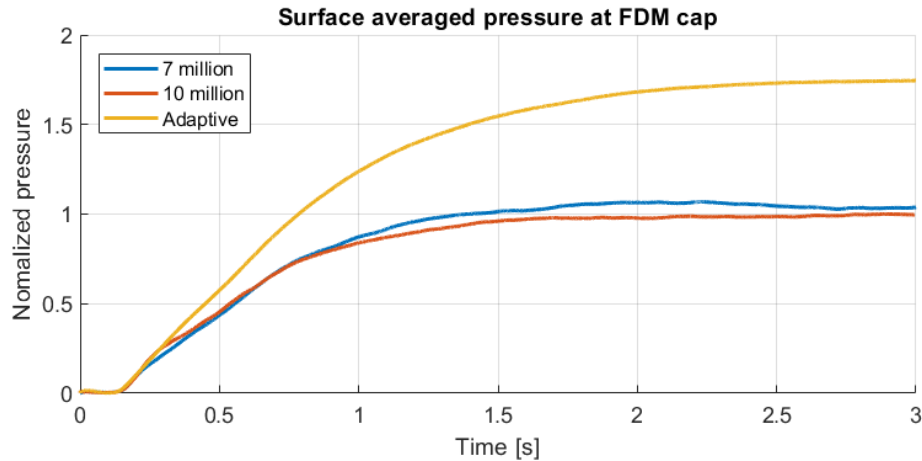
Figure 4.4: The normalized pressures for the different meshes, measured at the FDM cap.

The pressure in the tank was calculated as the surface average pressure at the FDM cap, which results can be seen in Figure 4.4. Time averaging the values over the last second of flow time gives a difference of 5.9% between the fine and coarser mesh, which is a little high. It is worth noting the trend of the results, which indicates that the difference between the meshes becomes smaller after 2.5 seconds. If the time averaging was done at another interval than than just the last second of flow time, the difference would probably be smaller than 5%.
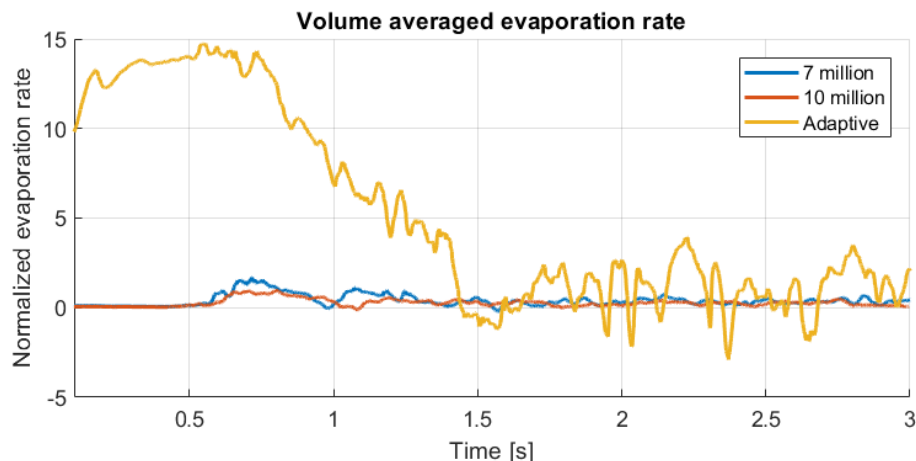
Figure 4.5: The normalized and volume averaged evaporation rate in the system for the three different meshes.

Looking at the overall evaporation rate inside the domain makes the mesh dependency study interesting. The evaporation rate is here calculated as a volume average

in the domain, which explains the low values, shown in Figure 4.5. Having a quick
look at the results, it seems like the fine and coarser mesh are generating almost
the same results, while the adaptive mesh is extremely bad in this case. Looking
closer at the differences between the two relevant meshes and time averaging the
values over the last second of flow time, large differences at approximately 63.4%
are discovered. With this result in mind, the accuracy of the fine mesh could also
be questioned when it comes to tracking vapours and evaporation in the tank. Be-
cause of the required time simulating the finer mesh, an even finer mesh could not
be investigated during the time frame of this project. Since the results of all other
parameters investigated are relatively close to each other, and the limited time in
the project in mind, it was decided that the coarser mesh of approximately 7 million
cells were accurate enough to generate reliable results, except from the evaporation
rate where none of the investigated meshes could be trusted to give reliable results.
With a larger time frame, even finer meshes would have been investigated in the
mesh dependency study, where the evaporation rate would have been a main target
to verify the dependency of the mesh resolution. It would also be suitable to cal-
culate the evaporation rate as a surface average at the fuel surface, which probably
would generate values closer to the measured evaporation rate in the experiments
described in Section 4.2.1.

4.2 Validation of implementation

The results of how the studied fuel evaporates in a simple geometry from the physical
experiments and simulations are shown and discussed below.

4.2.1 Experimental results

The evaporation rate was measured every minute for approximately an hour to verify
how the evaporation occurs in relation to time.
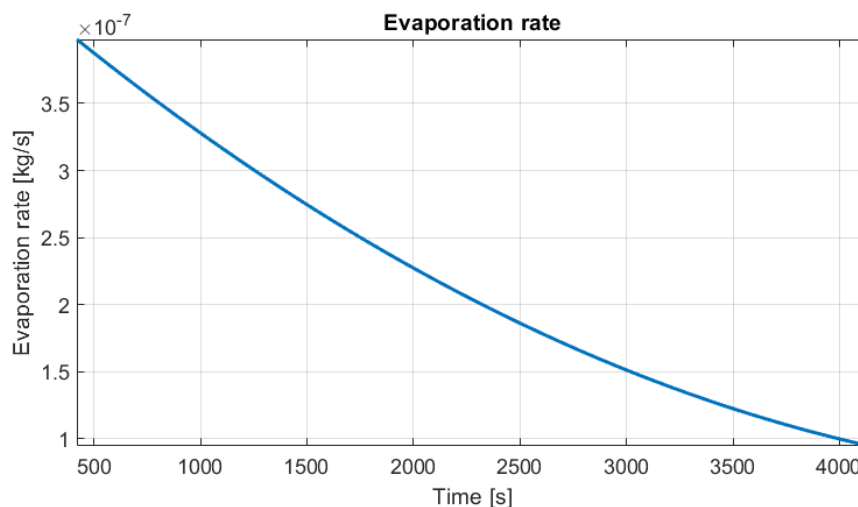
Figure 4.6: Measured evaporation rate in kg/s in relation to time for EPA Tier 3.

The first minutes were neglected to get rid of some measurement errors because of variations of the environmental changes during those minutes. The result of how the evaporation rate changes with time is shown in Figure 4.6. The measured results indicates that the lightest components of the gasoline is evaporated at a higher rate during the initial period of time, followed by a decreasing evaporation rate when the time increases.

4.2.2 Simulated experimental results

The results of the simulations in a simple geometry are shown in Figure 4.7.
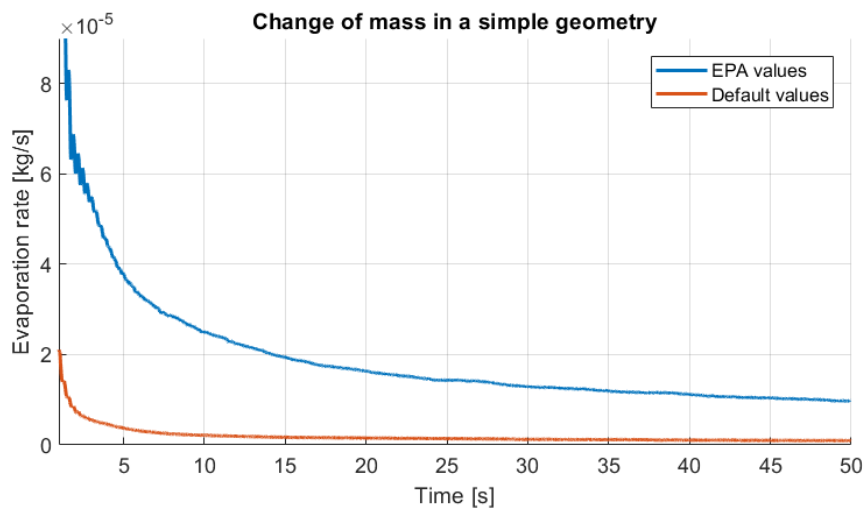
Figure 4.7: Simulated evaporation rate in kg/s in relation to time for EPA Tier 3 and default gasoline.

The simulations were run using both the measured values of the saturation pressure for EPA Tier 3 fuel and the default settings of the saturation pressure for gasoline in Star-CCM+. It is worth to note that the three-dimensional simulations only ran for 50 seconds, which is much shorter than the real experiments. The lighter components of the gasoline evaporates in the beginning of the process, which makes it hard to compare the results from the experiment with the simulations. The initial mass fraction of vapours in the gas phase consisted of 100% air because of the settings in the three-dimensional simulations of the ORVR system. As the results indicates, the evaporation of the default settings of the saturation pressure is lower than the rate of evaporation using the measured values of the EPA Tier 3 fuel. If the evaporation rate of the simulations are assumed to be rather constant with time even after the first 50 seconds, it might be seen that the rate of evaporation is a little higher in the simulations than in the reality. This assumption might make the default values fit even better to the experimental results (Figure 4.6). If the rate of evaporation instead becomes almost like the results of the experiments, the default values of the saturation pressure of the gasoline instead generates a lower evaporation rate than what is desired.
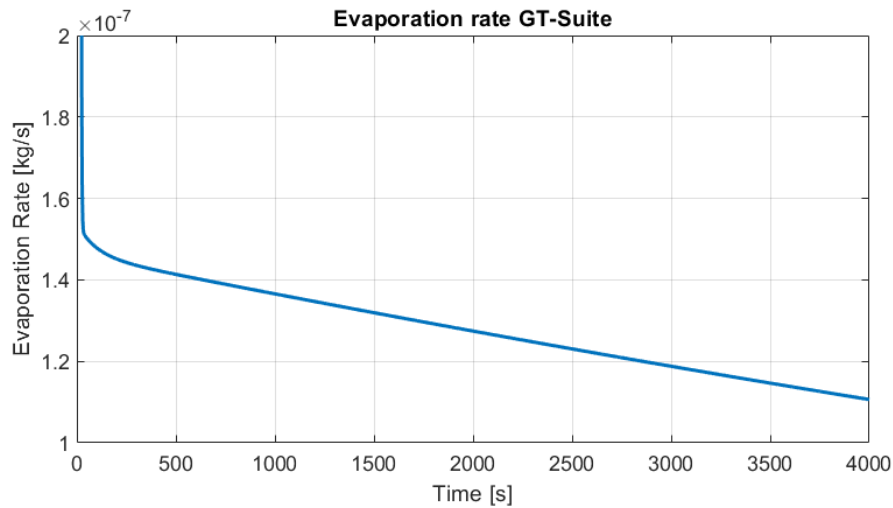
Figure 4.8: Measured evaporation rate in kg/s in relation to time for EPA Tier 3.

In the one-dimensional simulation in GT-Suite, it was possible to run the simulation during the same time frame as the experiment. The plot shown in Figure 4.8 indicates that the evaporation rate is high during the first seconds before it takes a value quite close to the experimental measurements. This corresponds quite well to the experimental measurements shown in Figure 4.6.

4.3 Results of simulations

The results from the simulations of the ORVR system are shown and discussed in the following section.

4.3.1 Pressure in upper tank

Figure 4.9 shows the pressure development in three-dimensions measured at the FDM-cap in the tank when the refuelling starts with 10% pre-fill.
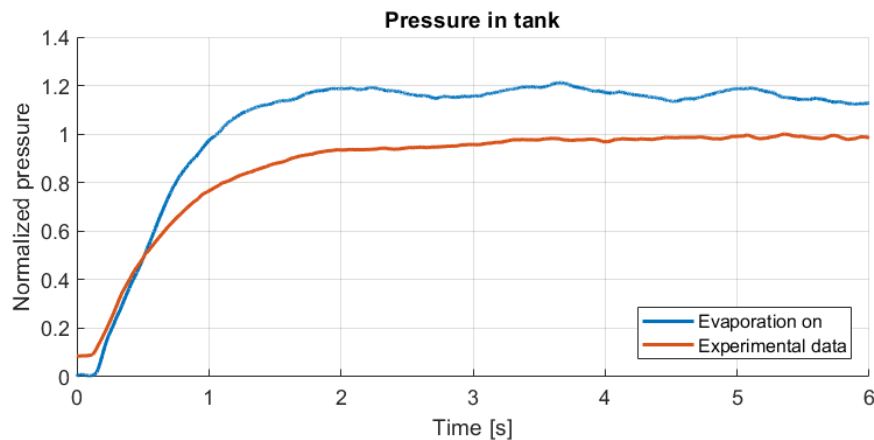
Figure 4.9: Results of pressure in tank from the three-dimensional simulation compared with experimental data.

The values from the simulation in Star-CCM+ were then compared with experimental data, measured at the top of the tank using the fuel EPA Tier 3. As can be seen, the values from the simulation generates higher values than the experimental data. It should be noted that the saturation pressure of the gasoline in the simulations do not correspond to the saturation pressure of EPA Tier 3, which is further explained in Section 3.2.1. This makes the comparison between the simulation and the experimental data hard to evaluate, since it is an important source of error. It is also important to note that the experimental results are all from the same test, so it would be beneficial to compare with a larger sample of data to really be able to draw further conclusions of the results.
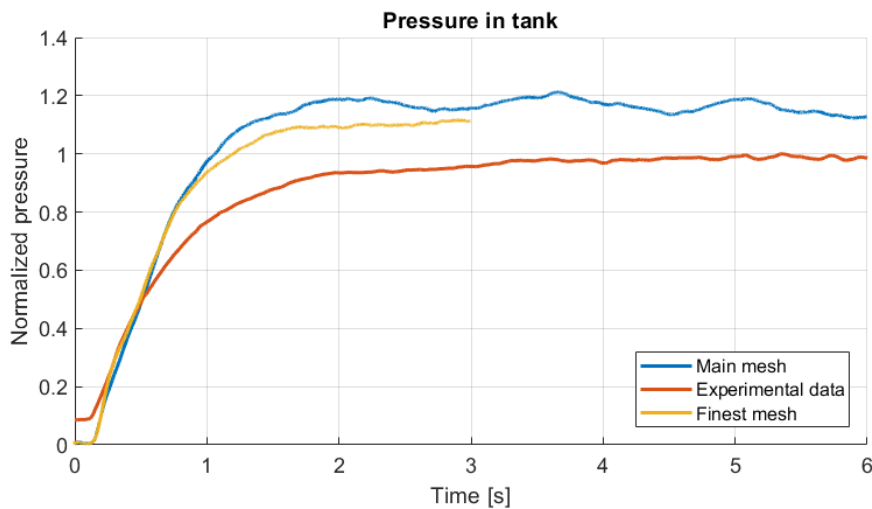
Figure 4.10: Results of pressure in tank from the three-dimensional simulation, compared with finer mesh and experimental data.

The pressure from the experimental data seems to increase with time while the pressure from the simulation stabilizes around a fix value, which would make it interesting to run the simulations for a longer time and verify if the values converges with an increased sample of values. The reason why the experimental data starts from a higher value than zero is that the values are exactly what the measuring instrument showed, and it did not start at zero when the experiment begun, possibly caused by the evaporation happening during the soaking process, before the experiment started. The gas phase in the simulations consisted of 100% air when the simulations started to increase stability, which is also a distinguishable difference between the results of the three-dimensional simulations compared to the experimental data.

Looking deeper at the results of the same measured pressure from the three-dimensional simulation at the FDM-cap, another source of error is discovered. Adding the results of the finer mesh investigated in the mesh dependency study, it appears that those results are closer to the experimental data, depicted in Figure 4.10. With the difference of the rate of evaporation between the meshes, discussed in Section 3.1.3.1, in mind, an even finer mesh would be interesting to evaluate towards the

experimental data. This could not be done during the limited time of the project.

4.3.1.1 Differences with and without evaporation

The results of the pressure at the FDM-cap from the three-dimensional simulation were also compared to a simulation with the same mesh and settings, but without any model for evaporation. The results of this comparison are shown in Figure 4.11. The plot indicates that the results of the simulation without evaporation generates lower values of the pressure than the simulation with evaporation included, which is expected because of the vapour development causing higher pressures.
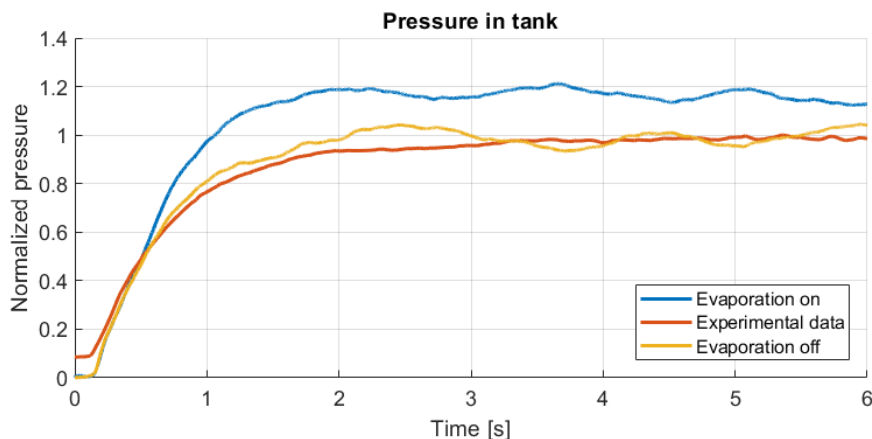
Figure 4.11: Results of pressure in tank from the three-dimensional simulation with and without evaporation, compared with experimental data

It is interesting to note that the values are close to the experimental data, which makes it tempting to draw the conclusion that a simulation without evaporation generates values closer to the reality. It is though important to remember that evaporation is occurring in reality, and a model with extended physics should in theory generate more reliable values, if correctly implemented. The difference in saturation pressure is not a source of error in the model without evaporation, which might reduce some sort of difference between the simulation and experimental data. Whether the differences between the simulations and the experimental data are caused by faults in the initialization or boundary conditions in the simulation setup could be further investigated, but no evident fault was discovered during the time of the project.

4.3.1.2 Comparison to one-dimensional simulation

Finally, adding the results from the one-dimensional simulation, we could in Figure 4.12 see that this gives the opposite relation towards the experimental data than the three-dimensional simulations. The one-dimensional simulation generates instead a pressure lower than the experimental data. It is important to remember that the pressure measured in the tank using the one-dimensional approach is based on

the average pressure in the entire tank, and not at any specified point as in the experiment or the three-dimensional simulations. The saturation pressure was also what was measured for the fuel EPA Tier 3, which could not be implemented into the three-dimensional simulation with evaporation, which might explain why the results are close to the experimental results according to the figure.
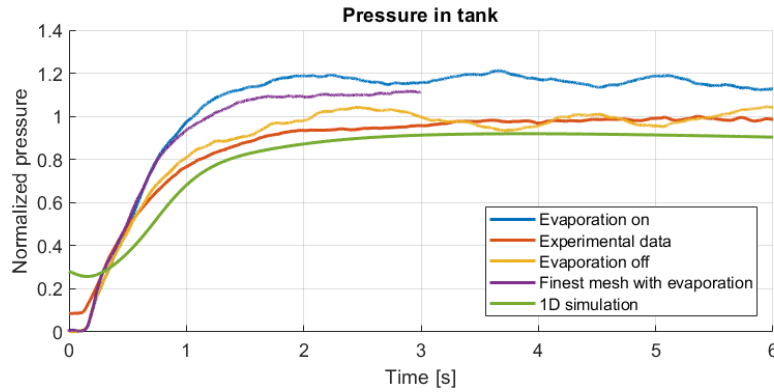
Figure 4.12: Results of pressure in tank from the three-dimensional simulation with and without evaporation, finer mesh and one-dimensional simulation using the FluidReservoir tank model compared with experimental data

4.3.2 Pressure in recirculation line

Pressures were picked from a surface about five pipe diameters from the first bend from the tank in the recirculation. The position can be seen as the shift between brown and green in Figure 3.9. The pressures are then plotted in Figure 4.13 for the different simulations.
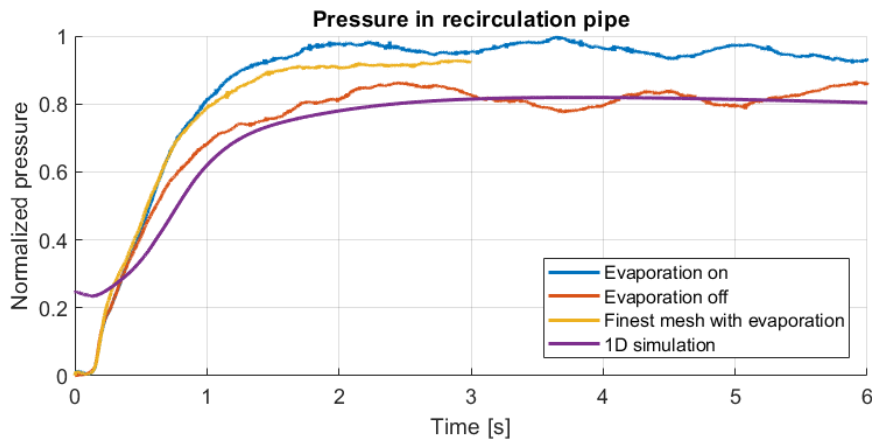
Figure 4.13: The pressure in the recirculation pipe taken at a position around five pipe diameters from the first bend from the tank connection. The one-dimensional simulation is done using the FluidReservoir tank model.

There exists no experimental measurements in the recirculation pipe so only simulation results are compared. In the figure the major thing to notice is that the

run without evaporation returns lower pressure than the runs with in the three-dimensional simulation. Also the finer mesh used in the mesh study gives results closer to the one without evaporation. The immediate evaluation of this is that it is very similar behaviour as the pressures in the tank earlier shown. Assuming the experimental values would also be similar, the same conclusion can be drawn: that an even finer mesh would likely give even better results. It is however not possible to judge the accuracy of results that an infinitely resolved mesh would give. The one-dimensional simulation seems to under predict the pressure in a similar way as in the tank. The pressure is measured at approximately the same position in the recirculation line between the different simulation approaches, which makes the comparison reasonable. The exact accuracy of those results could not be fully evaluated since no experimental data was provided, but it is interesting to note that the one-dimensional data are close to the simulation in three-dimensions without evaporation, which earlier was close to the experimental data.

4.3.3 Mass flow in recirculation line

The mass flow rate through the recirculation line are measured for the simulations with and without evaporation, the finer mesh and the one-dimensional simulation, which are all shown in Figure 4.14.
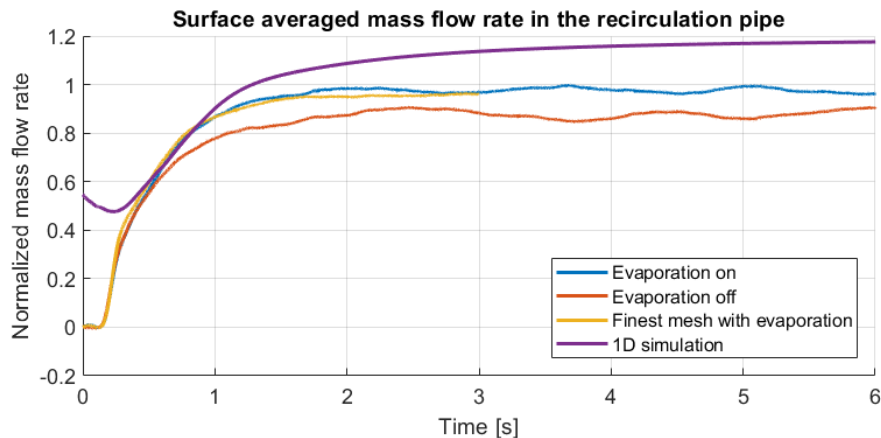
Figure 4.14: The mass flow rate of gas in the recirculation pipe, at around five diameters from the first bend after the tank. The one-dimensional simulation is done using the FluidReservoir tank model.

No experimental data was available for this measurement. The apparent behaviour is the same as before with the evaporation giving higher values, caused by the development of vapors. The difference is expected considering the pressures in the tank, and them being relative to a reference ambient pressure at the air inlet at the filler neck. This would drive the different flow rates seen in the plot. The results from the one-dimensional simulation are in this case higher than the three-dimensional simulations.

4.3.4 Mass flow through outlet

The mass flow in the outlet towards the canister, the LCO outlet, displayed in Figure 4.15. The behavior is overall the same as in the recirculation pipe. Once again, the mass flow rate are higher in the one-dimensional simulation compared to the three-dimensional cases.
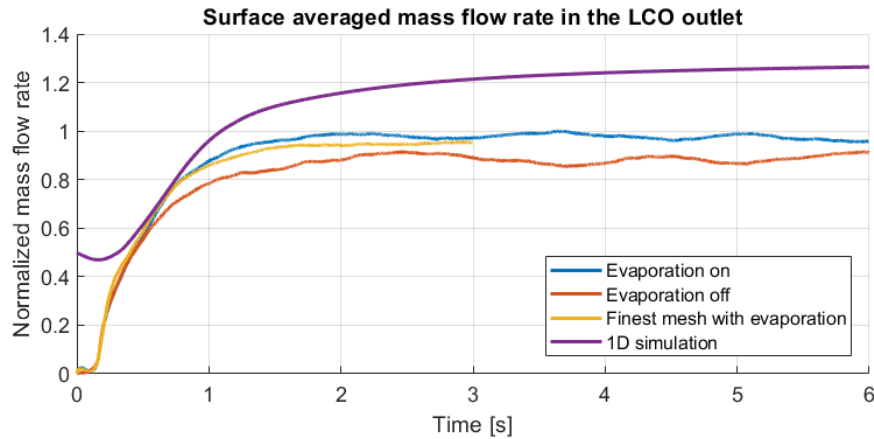
Figure 4.15: The mass flow rate of gas in the LCO outlet with and without evaporation, compared with the finest mesh from the mesh study and the one-dimensional simulation using the FluidReservoir tank model.

This might be caused by a possible higher evaporation rate in GT-Suite since the saturation pressure are the same as EPA Tier 3, which according to Figure 4.7 should result in a higher rate of evaporation in the simulations. A higher rate of evaporation in the domain could then generate an increased mass flow rate of vapours through the system, which might explain the higher mass flows in the one-dimensional simulation through the recirculation pipe and LCO outlet shown in 4.14 and 4.15, respectively.

4.4 Three-dimensional specific outputs

There are specific outputs from the three-dimensional simulations which are not possible to get in the one-dimensional simulation. Some of those are presented below.

4.4.1 Pressure distribution in filler pipe

The pressure distribution in the filler pipe at 3 seconds of flow time could be found in Appendix A.2 for both the low-fill case with and without evaporation, respectively. The volume fraction of gasoline at the same locations are also shown, which depicts where the fuel is located. There are no big differences between the cases, but the flow path differs a little which causes differences in the pressure distribution, which are especially seen at the lowest part of the pipes in the figures. This kind of result is an example of what a three-dimensional simulation can deliver, which are not possible in the one-dimensional setup.

4.4.2 Development and movement of vapours

The vapour development in the tank with 10% pre-fill at four different times are shown in Figure 4.16.

(a) 0.33s.

(b) 1.78s.

(c) 3.55s.
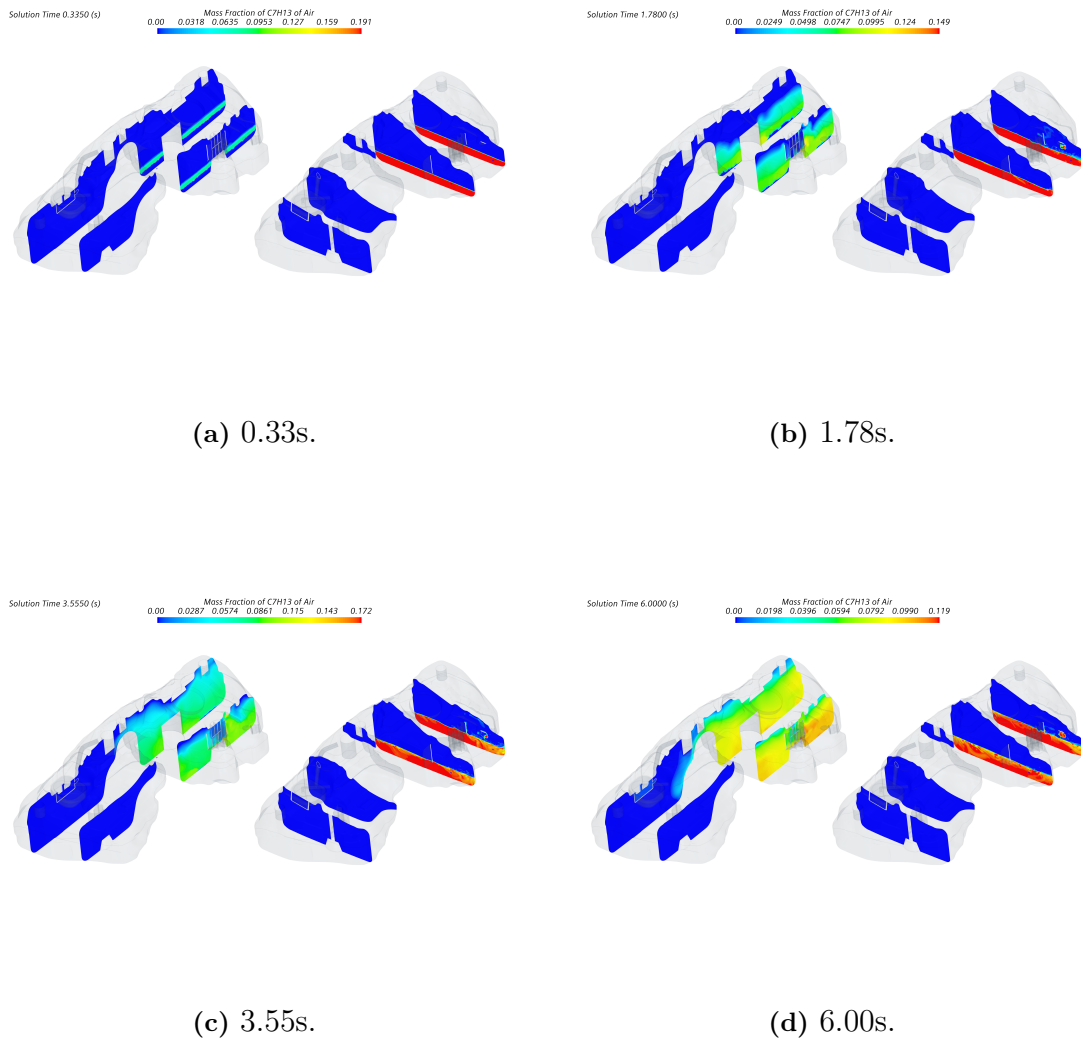
(d) 6.00s.

Figure 4.16: Development of evaporating fuel in the tank at 0.33s, 1.78s 3.55s and 6.00s with low pre-fill. To the left the vapours are shown, and to the right the volume fraction of gasoline.

The left part of each subfigure depicts the mass fraction of gasoline vapours in the gas phase of the domain, while the right part of each subfigure shows the volume fraction of gasoline in the domain, to give a feeling of the relation between vapour development and movement of the liquid. It can be seen that the vapours develop rather quick in the tank, especially where the fuel is injected and some sloshing occurs. The vapours enters the passive side of the domain after 6 seconds of fuel flow time, which indicates that the vapours probably reaches almost every possible part

of the domain within a complete refuelling process of approximately 100 seconds. This illustrates the need of implementation of evaporation in the simulation setup, since the vapours affects the measured pressures and the path of hydrocarbons in the system may be tracked.

4.5   One-dimensional specific outputs

Since the one-dimensional simulation is fast to run, an entire refuelling process can be simulated in approximately one hour. Figure 4.17 shows how the pressure in the tank behaves in the one-dimensional simulation compared to experimental data.
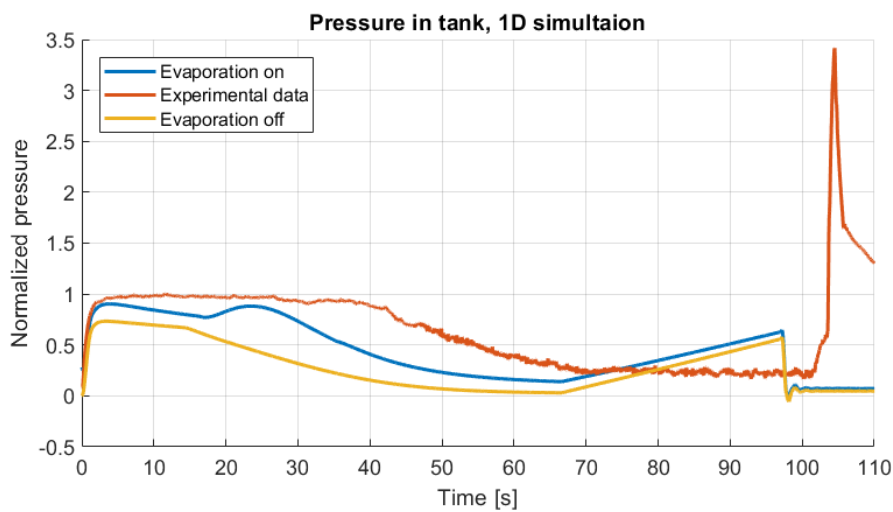
Figure 4.17: The one-dimensional and experimental pressures in the tank measured over the entire refuelling process, compared to the same one-dimensional simulation without evaporation. The simulation is done using the FluidReservoir tank model.

The last peak of the experimental data is caused by the fluid limit vent valve closing, which gives a pressure rise. The pressure decreases when the fuel flows over to the passive side of the tank at approximately 45 seconds of flow time in the experiments, which is happening at around 30 seconds in the one-dimensional simulation. The reason for this is probably the user-defined geometry of the tank, which becomes an approximation of what it is in the reality.

The same one-dimensional setup was also simulated without any model for evaporation, which results are also depicted in Figure 4.17. It can be seen that the development of vapours causes a higher pressure closer to the experimental results, as expected.

As discussed in Section 3.4.5, different setups were investigated in the one-dimensional simulation. The results from the one-dimensional simulation discussed are from the FluidReservoir model, but it is also interesting to compare results from other setups.

Figure 4.18 shows the pressure in the tank from both the FluidReservoir and Tank3D models in the one-dimensional simulation, compared to experimental results.
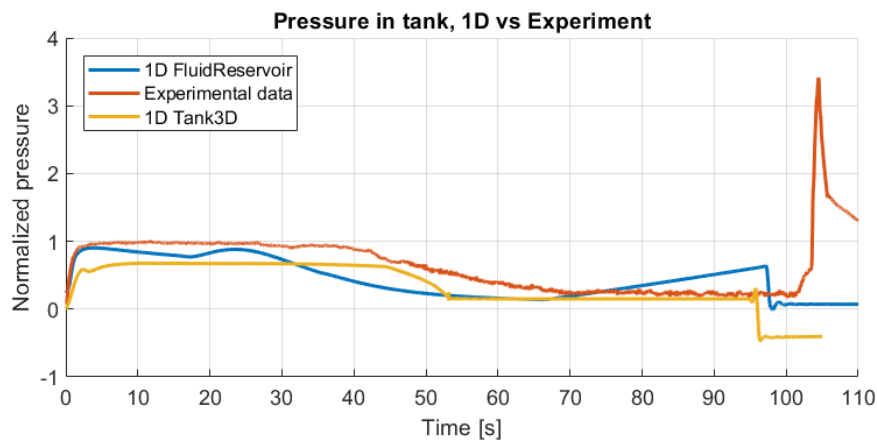
Figure 4.18: The one-dimensional simulation using the FluidReservoir tank model and experimental pressures in the tank measured over the entire refuelling process, compared with the results from the Tank3D model.

The Tank3D model mimics the geometry of the tank in a more detailed way, which explains why the overflow from the active to the passive side of the tank is more accurately captured in the Tank3D model compared to the FluidReservoir model, which occurs around 45 seconds after the refuelling has started with a low-filled fuel tank. If the Tank3D model was further developed, it would perhaps be a more suitable model for the future because of the more detailed geometry, but the model for evaporation could not be successfully implemented into the Tank3D model during the time of the project, which could explain why the measured pressures are lower than the results from the FluidReservoir model. It is important to note that the required time to simulate increases around 6 times when using the Tank3D model instead of FluidReservoir.

4.6 Comparison between one- and three-dimensional simulation

The main advantage of the three-dimensional simulation conducted in Star-CCM+ is the possible level of accuracy and the detailed approximation of the fuel flow phenomena of the ORVR system. The impact of the vaporized fuel could then be accurately evaluated and important sources of errors in the physical experiments could be detected and prevented by the use of a proper simulation. Possible changes to the fuel system could also be investigated, for example could the placement of the connection of the recirculation line into the filler neck be studied by examining the development of the pressure field inside the filler neck. The simulation could be used to conduct experiments that are expensive to perform in the reality. A change of the width or length of a pipe is hard to test in experiments but much smoother and cheaper in a computational setup.

A drawback of the three-dimensional simulation in Star-CCM+ is the required time and computational effort. It takes approximately 185 hours or about 8 days to simulate 1 second of flow time when using 200 cores on the cluster. The assumptions made to get a working simulation setup also makes the evaluation of the results hard to directly compare with experimental data at the moment, since the saturation pressure is set as the default settings of gasoline in the software Star-CCM+ and not the saturation pressure measured in experiments. If a solution of the problem with the change in saturation pressure is found in the future, it would be an even more efficient method of investigating the ORVR system.

The main drawback with the one-dimensional simulation is the loss in details of the results. It is important to understand that the one-dimensional setup does not resolve the entire complex and turbulent flow field in the same, more accurate, way as the three-dimensional case. This affects the results, and it should not be used in order to verify exact results towards the production or market. It is nevertheless an effective tool to test different initial settings and boundary conditions in order to get a feeling of how the changes will affect the results of the experiments or more detailed simulations in three-dimensions. The required time for simulating the entire refuelling process in one-dimension is about one hour, which makes it way faster than the more detailed simulations in Star-CCM+. The one-dimensional simulation setup conducted during this project could possibly be a first step in a test-cycle, where for example a geometry or other required input are changed and tested before being implemented in the three-dimensional simulations and physical experiments.

4.7 Clarifying benefits of simulations

To help the company understand the possible advantages and drawbacks with the different simulation setups, a one-pager was constructed, which is shown in Appendix A.4. The purpose of this is that engineers working with physical testing of the ORVR system should get an overview of what the simulations may be used to and what method to use in different situations. It is also a tool for the CAE-engineer working at the Fuel System Department to clarify what input is required to run the simulations and also the specific outputs from the different methods.

4.8 Possible ways to increase stability in the simulations

As mentioned in Section 2.5.2, the documentation of how Star-CCM+ treats the stability of evaporation in the solver is very insufficient. Other sources treating models for evaporation in other commercial softwares discusses the time scales of the convective and diffusive processes in an evaporating liquid. In the simulation setup, the time step was set as dependent on the CFL-number, which is regulated by

the convective transport in the system. The evaporating vapours is instead regulated by the diffusive transport in the system, which generates a changed time step [21]. According to [16], evaporation of droplets is often treated with a time step around 10^{-6} seconds while the global time step for the gaseous phase typically is around 10^{-4} seconds, which might cause issues with the coupling with the phases since they are solved at different time scales. In order to verify if the simulations would be possible to run with the desired saturation pressure of EPA Tier 3, a simulation with a very low time step would have to be investigated. Since the time of the project was limited, a time step around 10^{-6} seconds would have required too much computational time to be able to run and was therefore not investigated as a possible solution to the problem of treating the measured saturation pressure of EPA Tier 3 in the study.

4.9 Sources of errors

Some simplifications have been made during the study, which causes sources of errors in the simulations. Those are discussed below for both the one- and three-dimensional simulations, respectively.

4.9.1 One dimensional simulation

- The OPW filler pistol is an approximated shape. An axisymmetric flow region is changed into a bend with varying diameters, which should represent the active cross section area in one dimension of the complex flow path through the fuel pistol. An image of the geometry is shown in Figure 3.6.
- In the capless unit the different pipes positions are geometrically indistinguishable. This means that the flow can go down any of the pipes, at least in early states of development of the flow. At first, approximately 700g of fuel flow goes directly out through the air inlet. This is within the initialization time before the refuelling process is begun.
- Shapes in general are approximated compared to the three-dimensional simulations, since only the cross section area of the pipes are decisive and finer details are not considered.
- The tank especially has an approximated geometry, which is user defined.
- Gasoline is an approximation since it is assumed to be one homogeneous fluid.
- The filler pipe filled with fuel in the initialization in the one-dimensional simulation setup in order to increase the stability of the simulation.
- The passive side of the tank is pre-filled with a small amount of fuel (0.03% of the total volume) in the initialization to increase the stability of the simulation.

4.9.2 Three-dimensional simulation

- The geometry is simplified, with some finer details removed that were regarded as indecisive for the fuel flow.

- Gasoline is an approximation with default saturation pressure. It is also assumed as one homogeneous fluid and not a large number of combinations as in the reality.
- The initial mass fraction of gasoline vapours in the tank are set to 0% because of stability issues, which would have been set to approximately 60% in an ideal simulation setup. The experiments are instead performed in tanks where the evaporation has already started, causing vapours in the tank from the beginning of the measurements.
- A first order time integration scheme was used in order to enhance the stability of the simulation setup. Nevertheless, the accuracy of the results may be increased by using a second order time integration scheme, but this was not advisable from the Star-CCM+ support when simulating evaporation using VOF.

4.9.3 Mesh dependency of vapours

Since it appeared that the evaporation rate changed a lot between the investigated meshes, a further mesh dependency study is required to make sure that all the vapours are modelled. The accuracy of the movement of the vapours could be questioned in the current simulation setup, an issue which would be evaluated by comparing with an infinitely fine mesh which also requires infinite computational resources.

4.10 Final input from the Star-CCM+ support

During the entire project, continuous contact has being held with the support working with the software Star-CCM+ at Siemens. Before the study was ended, further input on how to improve the stability of the three-dimensional simulation setup was delivered, but it could not be fully analyzed during the time frame of the project. It was discovered that a simulation setup with the measured saturation pressure of EPA Tier 3 could be run without having a crash during the first seconds of flow time, by changing the VOF-scheme from HRIC (High Resolution Interface Capture) to a first-order scheme and reducing the evaporation/condensation relaxation factor to from 1.0 to 0.7. However, this resulted in very inaccurate results of the measured pressures in the domain during the simulated time, which made the setup unsuitable for the case.

There was also a thought that the mesh was the cause of the instability when the measured values of the saturation pressure was used. Therefore, a mesh treating the dimensionless wall distance y^+ to always stay within $y^+ < 30$ was created, while also decreasing the evaporation/condensation and VOF relaxation factors to 0.1. The results of this simulation were not possible to fully investigate during the limited time of the project, but it was found that the simulation crashed after about 1 second of flow time, which meant that the simulation was able to run for a longer time than before. Figure 4.19 shows how the pressure in the tank developed during the only

managed simulated second of flow time. It can be seen that the simulation with the correct saturation pressure generated a lower pressure than the other simulations before it crashed, which might indicate that the results would have had a better accuracy towards the experimental results with the correct saturation pressure implemented. Further development of the simulation setup was required to be made in able to run without diverging, which was not possible within the project time frame.
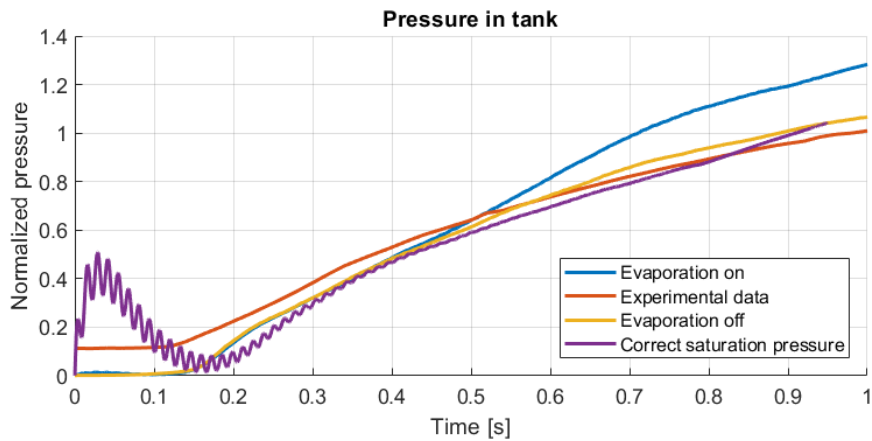

Figure 4.19: Development of pressure in the tank during the first second of flow time. A comparison between the stability improved setup with a correct saturation pressure and the earlier simulations.

5

Conclusion and future work

The main goal of the study was to implement a model for evaporation in the three-dimensional simulation to be able to track movement of vapours and mimic the physical experiments done of the ORVR system at the Fuel System Department. This was achieved, but with the limitation of using the default saturation pressure of gasoline inbuilt in the software Star-CCM+, which made it difficult to compare the experimental data towards the three-dimensional simulations in a fair way. It was not possible to find a working simulation with the measured values of the saturation pressure of the EPA Tier 3 fuel within the time frame of the project. A one-dimensional simulation setup of the ORVR system was also conducted, which might be a useful tool in order to quickly understand how changes to the required input parameters could affect the results of the experiments and three-dimensional simulations.

The results of the different simulation methods differed, with the one-dimensional setup generating results closer to the analyzed experimental data. The three-dimensional simulation differed compared to the data from physical experiments. An even finer mesh than those investigated in the mesh dependency study would have been interesting to evaluate in order to verify if the differences were caused by the mesh accuracy or if it was a result of the difference in saturation pressure or any other initialization error.

5.1   Suggested future work

The following section consists of items suggested as further development of the one- and three-dimensional simulation that were not included in the simulation setups.

5.1.1   One-dimensional simulation

- The user defined geometry of the tank could be further developed to imitate the real fuel tank as accurate as possible.
- The discretization of the capless filler neck could be further investigated.
- The Tank3D model could be further investigated, where a successful implementation for evaporation could generate interesting results.

5.1.2 Three-dimensional simulation

- Further increase the simulation stability to be able to initialize a simulation with appropriate mass fraction of vapours in the domain.
- Further development of the simulation setup to be able to run with the right saturation pressure. This could possibly be solved by using an even lower time step or possibly by improving the mesh even further.
- Extend the mesh study in order to ensure that the vapour movement are correctly modelled.
- The current simulation setup is very time consuming. It would be interesting to further explore the adaptive mesh feature in order to try to find the optimal mesh regarding both accuracy and required computational time.
- If it comes a possibility to couple multiphase problems in Star-CCM+ with GT-Suite in the future, it would be interesting to investigate this in order to save computational time. This is today only possible to do with single-phase problems.
- One possibility to decrease run time would be to run iterations and time steps on the evaporation calculations only. As an example to run 100 smaller time steps only calculating the evaporation equation and other equations on the small time scale, and then doing the main larger time step with the heavier calculations.
- The turbulence models could be further investigated, for example could LES be tested to verify if the accuracy of the results change.

Bibliography

[1] Riström A. Naronikar A. Cfd and experimental study of refuelling and venting a fuel system. Technical report, Linköping University, Luleå University of Technology, Linköping, 2019.

[2] EPA. Onboard refueling vapour recovery (orvr) regulations for light-duty vehicles and trucks and heavy-duty vehicles: Summary and analysis of comments. Technical report, United States Environmental Protection Agency, 1994.

[3] John D. Anderson Jr. *COMPUTATIONAL FLUID DYNAMICS: The Basics with Applications.* McGraw-Hill, Inc., New York, 1995.

[4] Malalasekera W. Versteeg H.K. *An introduction to Computational Fluid Dynamics, 2nd ed.* Pearson Education Limited, Edinburgh, 2007.

[5] SiemensPLM. *Simcenter STAR-CCM+ User Guide*, 2020. `https://documentation.thesteveportal.plm.automation.siemens.com/starccmplus_latest_en/index.html#page/STARCCMP%2FGUID-CDA9600B-F19D-46C2-9F8D-F13F0AAE012E.html%23`.

[6] Kravtsov A.V. Gnedin N.Y., Semenov V.A. Enforcing the courant friedrichs lewy condition in explicitly conservative local time stepping schemes. *Journal of Computational Physics*, (359):93–105, 2018.

[7] Davidsson L. Fluid mechanics, turbulent flow and turbulence modeling. Technical report, Division of Fluid Dynamics, Department of Mechanics and Maritime Sciences, Chalmers University of Technology, Gothenburg, 2020.

[8] SiemensPLM. *Simcenter STAR-CCM+ User Guide*, 2020. `https://documentation.thesteveportal.plm.automation.siemens.com/starccmplus_latest_en/index.html#page/STARCCMP/GUID-82CD7ECC-1BB5-4DA1-B024-273814BB8E3D.html`.

[9] Gersten K. Schlichting H. *Boundary-layer theory, Ninth ed.* Springer, Braunschweig, 2017.

[10] SiemensPLM. *Simcenter STAR-CCM+ User Guide*, 2020. `https://documentation.thesteveportal.plm.automation.siemens.com/starccmplus_latest_en/index.html#page/STARCCMP/GUID-478651F1-9901-41B6-8193-3052E3CCE9DB.html`.

[11] SiemensPLM. *Simcenter STAR-CCM+ User Guide*, 2020. `https://documentation.thesteveportal.plm.automation.siemens.com/starccmplus_latest_en/index.html#page/STARCCMP/GUID-38575333-1AB5-428D-B594-58D97DFB729A.html`.

[12] SiemensPLM. *Simcenter STAR-CCM+ User Guide*, 2020. `https://documentation.thesteveportal.plm.automation.`

`siemens.com/starccmplus_latest_en/index.html#page/STARCCMP/`
`GUID-9FA04457-47C5-4BC4-8B89-F67D3DC5E4F1.html`.

[13] Kallio S. Manninen M. Veikko V. On the mixture model for multiphase flow. Technical report, Technical Research Centre of Finland, Åbo Akademi, Åbo, 1996.

[14] Issa R.I. Ubbink O. A method for capturing sharp fluid interfaces on arbitrary meshes. *Journal of Computational Physics*, (153):26–49, 1999.

[15] M.; Sames P; Schelin T Muzaferija, S.; Peric. A two-fluid navier-stokes solver to simulate water entry. *Twenty-Second Symposium on Naval Hydrodynamics*, (22):640,641, 1998.

[16] S.S Sazhin. Advanced models of droplet heating and evaporation. *Progress in Energy and Combustion Science*, (32):162–214, 2006.

[17] SiemensPLM. *Simcenter STAR-CCM+ User Guide*, 2020. `https://documentation.thesteveportal.plm.automation.`
`siemens.com/starccmplus_latest_en/index.html#page/STARCCMP%`
`2FGUID-BF37DEC9-DCFB-E2F8-4A73-B4C2-14138D71ADA8.html%23`.

[18] Gamma Technologies. *GT-Suite Flow Manual*, 2020.

[19] Wondra F. Hardt S. Evaporation model for interfacial flows based on a continuum-field representation of the source terms. *Journal of Computational Physics*, (227):5871–5895, 2008.

[20] EPA. Hydrocarbon composition of gasoline vapour emissions from enclosed fuel tanks. Technical report, United States Environmental Protection Agency, 2011.

[21] Weigand B. Schlottke, J. Direct numerical simulation of evaporating droplets. *Journal of Computational Physics*, (227(10)):5215–5237, 2008.

[22] Grabner Instruments. *MiniVap VPXpert*, 2020. `https:`
`//www.grabner-instruments.com/products/vapor-pressure/`
`minivap-vpxpert-vapor-pressure-tester`.

[23] SiemensPLM. *Simcenter STAR-CCM+ User Guide*, 2020. `https://documentation.thesteveportal.plm.automation.`
`siemens.com/starccmplus_latest_en/index.html#page/STARCCMP%`
`2FGUID-4A2D8031-4363-46E4-8F25-9A90F2359463.html%23`.

[24] SiemensPLM. *Simcenter STAR-CCM+ User Guide*, 2020. `https://documentation.thesteveportal.plm.automation.`
`siemens.com/starccmplus_latest_en/index.html#page/STARCCMP%`
`2FGUID-AD2B8BC3-5C37-4F9D-9F42-0ED4C372C711.html%23`.

[25] SiemensPLM. *Simcenter STAR-CCM+ User Guide*, 2020. `https://documentation.thesteveportal.plm.automation.`
`siemens.com/starccmplus_latest_en/index.html#page/STARCCMP%`
`2FGUID-46C343ED-DCFB-4EBB-83BF-90EE5DBCE7D1.html`.

[26] SiemensPLM. *Simcenter STAR-CCM+ User Guide*, 2020. `https://documentation.thesteveportal.plm.automation.`
`siemens.com/starccmplus_latest_en/index.html#page/STARCCMP/`
`GUID-478651F1-9901-41B6-8193-3052E3CCE9DB.html`.

[27] SiemensPLM. *Simcenter STAR-CCM+ User Guide*, 2020. `https://documentation.thesteveportal.plm.automation.`

56

```
siemens.com/starccmplus_latest_en/index.html#page/STARCCMP/
GUID-812361C5-EEF9-4028-8A9C-EF5F730917B6.html.
```

[28] SiemensPLM.   *Simcenter   STAR-CCM+   User   Guide*,   2020.
```
https://documentation.thesteveportal.plm.automation.
siemens.com/starccmplus_latest_en/index.html#page/STARCCMP/
GUID-112029FC-12E0-426F-85FC-4198DE68A414.html.
```

[29] SiemensPLM.   *Simcenter   STAR-CCM+   User   Guide*,   2020.
```
https://documentation.thesteveportal.plm.automation.
siemens.com/starccmplus_latest_en/index.html#page/STARCCMP%
2FGUID-35E49124-899C-42C5-94BE-32D0A1278872.html%23.
```

[30] Wu J. Liu Z. Wang, F. Surface tensions of mixtures of diesel oil or gasoline and dimethoxymethane, dimethyl carbonate, or ethanol. *Energy Fuels - ENERG FUEL*, (20).

[31] SiemensPLM.   *Simcenter   STAR-CCM+   User   Guide*,   2020.
```
https://documentation.thesteveportal.plm.automation.
siemens.com/starccmplus_latest_en/index.html#page/STARCCMP/
GUID-AD444CAC-8F38-4825-8F38-EE6FA6EFDEF7.html.
```

A
Appendix

A.1   Gasoline EPA Tier 3

II

Haltermann Carless

VOLVO CAR CORPORATION
SE00012917
SEPV
BP2TU
VCC GODSMOTTAGNINGEN PVOE
SE-405 31 GOETEBORG

Certificate 100000159344

Date:	13.03.2019
Customer PO:	4150522095 (2205)
Delivery Note:	80137179 000010
Order No.:	66129548 000010
Customer No.:	1707081

GMID:	378805
Material:	Gasoline, EPA Tier 3 - E10 Premium (General Testing)
	149 KG LINED STEEL DRUM 1A1
Cust. Mat.:	8752775
Batch:	HA2903KK02
Orig. Batch:	
Sample No.:	30039978
Analyzed:	01.02.2019
Dlvy. Qty:	2.235,0 KG

Vehicle:	UPE 927 / HL-EL 1234		
Ship from:	Shipping Point Hamburg	Hamburg 02 Germany	Page: 1 / 2

Feature	Units	Results	Limits Minimum	Maximum	Method
(RON+MON)/2 (*[1])		94,2	91,0		ASTM D2699/D2700:2018a
Sensitivity (*[1])		11,4	7,5	-	ASTM D2699/D2700:2018a
Density at 15℃	kg/m3	751,6			ASTM D4052:2018
Specific Gravity at 60/60		0,7516			ASTM D4052:2018
DVPE	kPa	62,0	60,0	63,4	ASTM D5191:2018
DVPE	psi	9,0	8,7	9,2	ASTM D5191:2018
Distillation IBP	℃	37,5			ASTM D86:2018
Distillation IBP	℉	99,5			ASTM D86:2018
Dist. 10% v/v	℃	55,2	49,0	60,0	ASTM D86:2018
Dist. 10% v/v	℉	131,4	120,0	140,0	ASTM D86:2018
Dist. 50% v/v	℃	95,0	88,0	99,0	ASTM D86:2018
Dist. 50% v/v	℉	203,0	190,0	210,0	ASTM D86:2018
Dist. 90% v/v	℃	164,2	157,0	168,0	ASTM D86:2018
Dist. 90% v/v	℉	327,6	315,0	335,0	ASTM D86:2018
Distillation FBP	℃	194,1	193,0	216,0	ASTM D86:2018
Distillation FBP	℉	381,4	380,0	420,0	ASTM D86:2018
Dist. Residue	%(V)	0,5	-	2,0	ASTM D86:2018
Sulfur	mg/kg	10,3	8,0	11,0	ASTM D5453:2016
Total Aromatics	%(V)	22,6	21,0	25,0	ASTM D5769:2015
C6 Aromatics	%(V)	0,6	0,5	0,7	ASTM D5769:2015
C7 Aromatics	%(V)	5,5	5,2	6,4	ASTM D5769:2015
C8 Aromatics	%(V)	5,5	5,2	6,4	ASTM D5769:2015

Haltermann Carless

VOLVO CAR CORPORATION	Delivery item/date	Page
VCC GODSMOTTAGNINGEN PVOE	80137179 000010 / 18.03.2019	2 / 2
SE-405 31 GOETEBORG		

Feature	Units	Results	Limits Minimum	Maximum	Method
C9 Aromatics	%(V)	5,8	5,2	6,4	ASTM D5769:2015
C10+ Aromatics	%(V)	5,2	4,4	5,6	ASTM D5769:2015
Olefins	% w	5,4	4,0	10,0	ASTM D1319:2018
Olefins	% w	5,2			ASTM D6839:2018
Ethanol	%(V)	9,70	9,40	10,20	ASTM D4815:2015b
Ethanol	%(V)	9,8	9,6	10,0	Blended
Other Oxygenates	%(V)	< 0,10	-	0,10	ASTM D4815:2015b
Oxygen Content	% w	3,57			ASTM D4815:2015b
Oxidation Stabilit (*[1])	min.	> 1200	1000	-	ASTM D525:2012a
Solvent Washed Gum	mg per 100mL	< 1,0	-	3,0	ASTM D381:2012
Corrosion - Copper	-	1A Max. 1	-	-	ASTM D130:2018
Lead	g/l	< 0,0026	-	0,0026	ASTM D3237:2017
Phosphorus (*[1])	g/l	< 0,0002	-	0,0013	ASTM D3231:2013
Water	mg/kg	206	-	-	ASTM D6304:2016
Carbon Content (*[1])	% w	82,7			ASTM D5291:2016
Hydrogen Content (*[1])	% w	13,60			ASTM D5291:2016
Oxygen Content	% w	3,7	-	-	Calculated
C:H Ratio (H=1)		6,08			Calculated
H:C Ratio (C=1)		0,164			Calculated
Net Heating Value (*[1])	MJ/kg	41,990			ASTM D240:2017
Net Heating Value (*[1])	Btu/lb	18052			ASTM D240:2017

(*[1]) : tested by subcontractor
(*[2]) : not accredited
(*[3]) : modified

The certificate is electronically generated and valid without signature.

The analyses were conducted in our DIN EN ISO/IEC 17025 accredited laboratory.
Robert Geisler, Phone ++49-40-33318-149
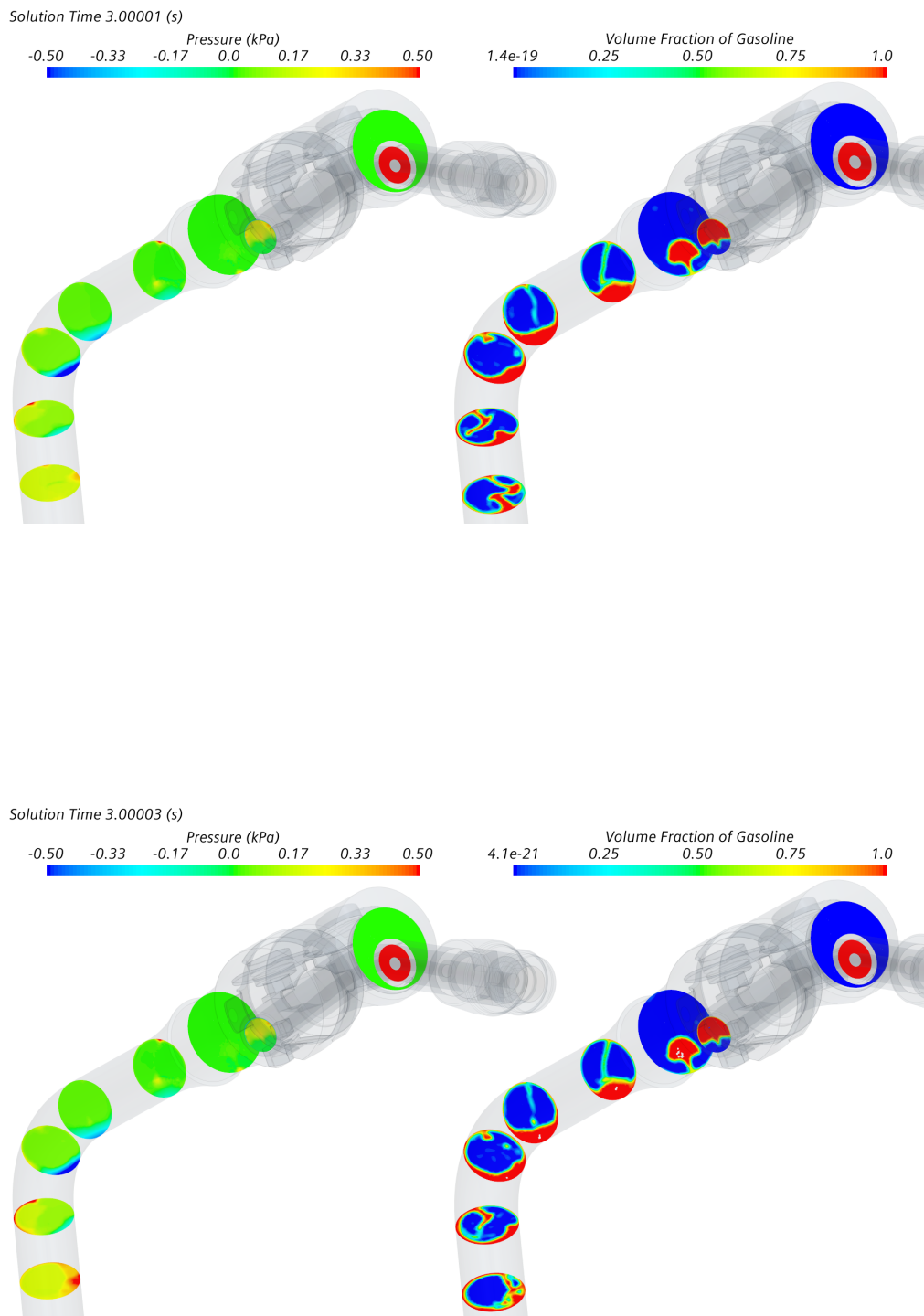
A.2 Pressure distribution in filler pipe

Figure A.1: Pressure distribution in the filler pipe at 3 seconds, with evaporation in the upper figure and without evaporation in the lower.

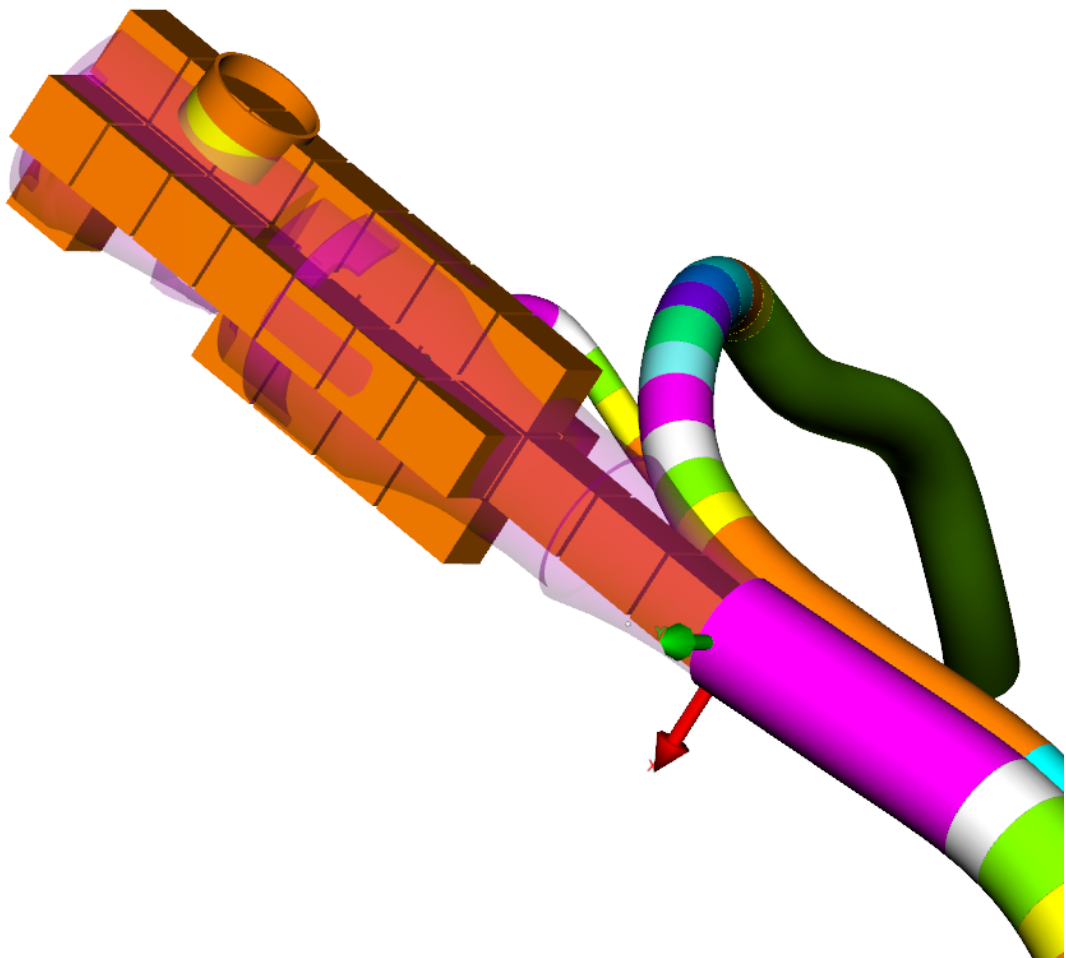## A.3   One dimensional discretization variations

Figure A.2: A visualization of the discretization of the capless filler neck.
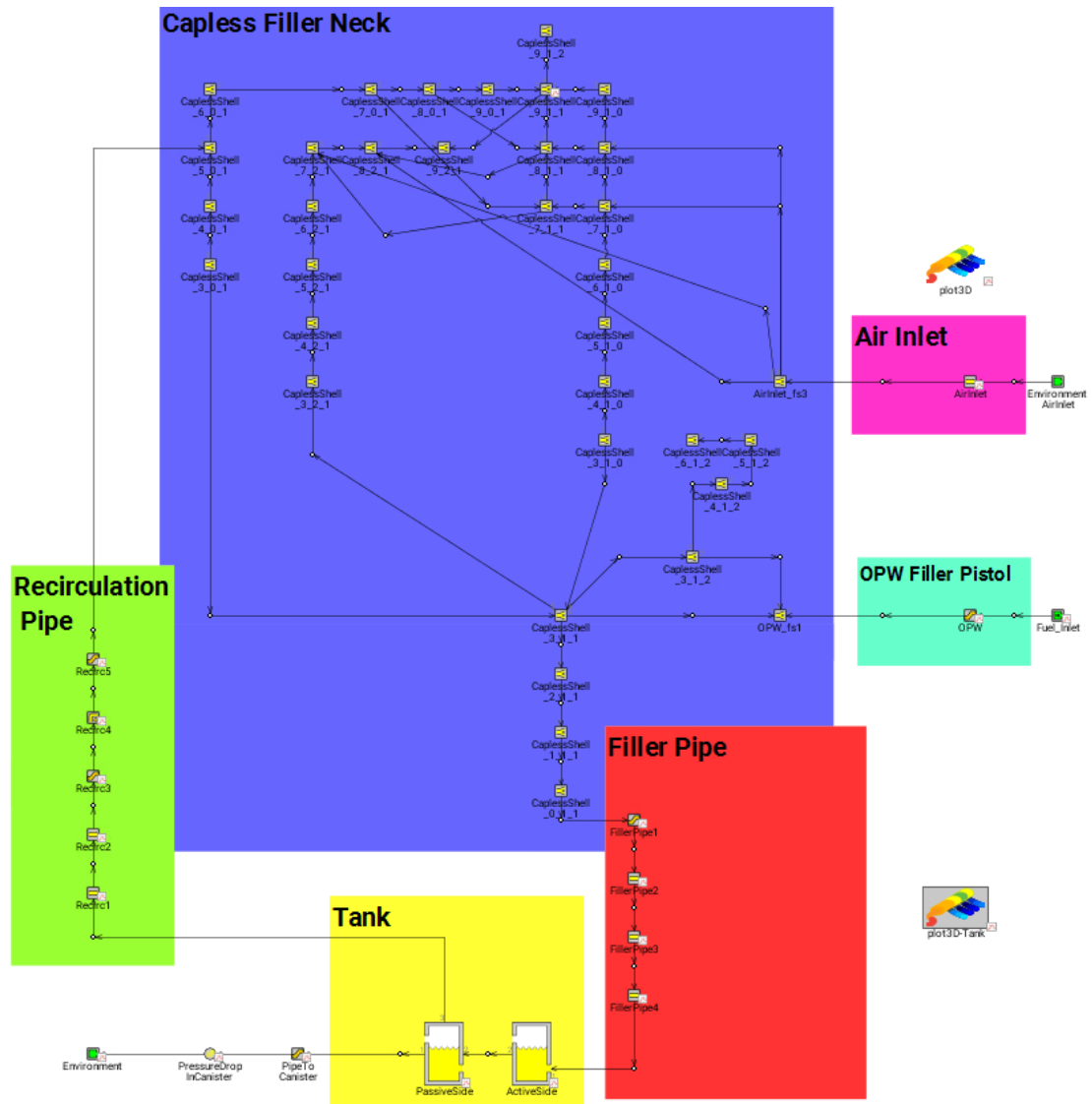
Figure A.3: The full ORVR system implemented in GT-Suite based on the finer discretization.

A.4   OnePager

Computational fluid dynamics (CFD)
- Simulations on the ORVR system

Required input variables

- Fuel pistol flowrate
- Temperature of fuel in tank
- Temperature of fuel in pistol
- Temperature of environment
- Initial fuel volume in tank
- Pressure drop over canister
- CAD files of the components
- Fuel type

Output variables

- Pressure in all components
- Temperature in all components
- Rate of evaporation
- Mass flow through all components
- Fuel volume in tank

3D specific advantages

- Flow phenomena
- Velocity fields everywhere
- Pressure fields everywhere
- Position and movement of vapours

3D specific drawbacks

- Requires 37 000 CPU hours per second of simulated time ≈ 185h on 200 cores per second of simulated time
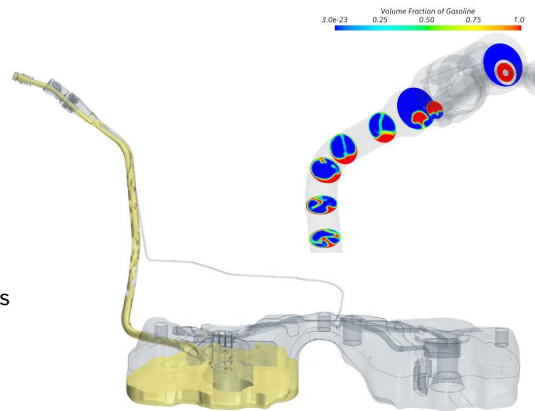
1D specific advantages

- An entire refuelling process could be run in less than one hour

1D specific drawbacks

- Mean values of every studied variable in every component